1 Title Page

A Comprehensive Treatment-Induced Resistance Atlas of Glioblastoma Reveals a Fibrotic Niche Shielding the Tumor from Immunotherapy

Fei Wang[1,*], Run Huang[2], Hongyi Ling[2], Yuhan Bai[2], Chen Yang[1], Guozheng Zhao[1], Xin Wu[1], Wenqian Cao[2], Yue Lu[1], Yining Zhang[2], Dengfeng Lu[1], Youjia Qiu[1], Juyi Zhang[1], Bixi Gao[1], Chao Ma[1], Hanhan Dang[3], Yulian Zhang[3], Yanbo Yang[4], Ting Sun[1], Zhouqing Chen[1,*], Zhong Wang[1,*]

Institutional affiliations

1 Department of Neurosurgery& Brain and Nerve Research Laboratory, The First Affiliated Hospital of Soochow University, Suzhou, Jiangsu Province, 215006, China

2 Suzhou Medical College of Soochow University, Suzhou, Jiangsu Province, 215127, China

3 Department of Neurosurgery, China-Japan Friendship Hospital, Chinese Academy of Medical Sciences & Peking Union Medical College, Beijing, 100000, China

4 Department of Oncology, Division of Pediatric Oncology, Johns Hopkins School of Medicine, Baltimore, Maryland

E-mails of the authors:

Fei Wang: wangfeineu@163.com; Run Huang: 2713315776@qq.com; Hongyi Ling: 482697159@qq.com; Yuhan Bai: 1367732191@qq.com; Chen Yang: yangelababy007@163.com; Guozheng Zhao: zgz1340788047@163.com; Xin Wu: wuxin112340@163.com; Wenqian Cao: 2430805008@stu.suda.edu.cn; Yue lu: 2552926527@qq.com; Yining Zhang; 2245998942@qq.com; Dengfeng Lu: 544821174@qq.com; Youjia Qiu: qiu_youjia@163.com; Juyi Zhang: zhangjuyi123456@163.com; Bixi Gao: gaobixi140508@163.com; Chao Ma: machaoss@163.com; Hanhan Dang: nsdhh5124@pumc.edu.cn; Yulian Zhang: zhangyulian@pku.edu.cn; Yanbo Yang: yangyb6@outlook.com; Ting Sun: sunting@suda.edu.cn

* Correspondence:

Fei Wang

wangfeineu@163.com

Zhouqing Chen

zqchen6@163.com

Zhong Wang

wangzhong761@163.com

2 Abstract

Therapeutic resistance in IDH-wildtype glioblastoma (GBM) is driven by profound cellular plasticity and a structured immunosuppressive tumor microenvironment (TME). Here, we present the Glioblastoma Resistance Insights from Treatment Atlas (GRIT-Atlas), the most comprehensive single-cell resource to date, encompassing nearly one million cells from 296 samples across primary and recurrent cohorts, including those treated with immune checkpoint blockade (ICB) and anti-angiogenic combination therapy. We identify a convergent evolutionary trajectory where therapeutic pressure selects for a specific malignant state, cNMF7 (MES-like), characterized by a synergy of hypoxia, stemness, and inflammatory signaling. Integrating spatial transcriptomics across 48 patient sections, we define a "Spatial Resistance Triad"—a core functional unit composed of cNMF7 cells, differentiation-arrested E-MDSCs, and Type VI Collagen-secreting myCAFs. This triad specifically colonizes the hypoxic microvascular proliferation (MVP) and pseudopalisading necrosis (PAN) niches. Mechanistically, we show that myCAFs act as stromal architects, constructing a fibrotic scaffold through a Collagen/Fibronectin-CD44 signaling axis. This spatial infrastructure not only physically excludes cytotoxic T cells but also provides essential cues to sustain malignant plasticity and myeloid-mediated immunosuppression. Our findings across seven independent cohorts and pan-cancer validation underscore the clinical significance of this axis in driving immunotherapy failure. Collectively, the GRIT-Atlas provides a blueprint for dismantling the "immunosuppressive sanctuaries" of GBM to overcome therapeutic resistance.

Keywords: Glioblastoma (GBM), Single-cell RNA sequencing (scRNA-seq), Spatial transcriptomics, Immunotherapy resistance, Cancer-associated fibroblasts (myCAF), Myeloid-derived suppressor cells (E-MDSC) , Glioma stem cells (GSC), Hypoxia niche

3 Introduction

IDH-wildtype glioblastoma (GBM) represents the apex of therapeutic resistance among primary brain malignancies[1]. Despite an aggressive standard-of-care (SOC) regimen involving maximal safe resection followed by radiotherapy and temozolomide, recurrence is inevitable, resulting in a dismal median survival of approximately 15 months[2,3]. This intractability stems not merely from a static immunosuppressive microenvironment, but from the profound cellular plasticity and heterogeneity inherent to GBM[4,5]. Malignant cells exist as a dynamic ecosystem, capable of transitioning between functional states—ranging from neurodevelopmental to injury-response phenotypes—to evade therapeutic pressure[6,7]. However, the specific evolutionary trajectories driven by distinct therapeutic modalities, particularly how treatment actively reshapes the cellular hierarchy to favor resistant phenotypes, remain poorly defined.

The promise of immune checkpoint blockade (ICB) in GBM has been tempered by phase III clinical failures, necessitating a deeper interrogation of resistance mechanisms[8,9]. While the genomic landscape of primary versus generic recurrent tumors is well-charted[10,11], and inquiries into ICB responses are accumulating[12-14], there remains a paucity of systematic studies that definitively delineate the perturbation landscapes specific to standard of care, ICB, and combinatorial targeted therapies. Crucially, these cellular perturbations do not occur in isolation but within the highly organized spatial architecture of the tumor microenvironment (TME)[15-17]. As the TME functions as a structured ecosystem rather than a disordered collection of cells, understanding how diverse therapeutic stresses specifically reconfigure spatial neighborhoods to orchestrate immune exclusion represents a critical knowledge gap.

We hypothesized that the resistance to immunotherapy is physically anchored within specific histological niches. GBM is pathologically defined by two hallmark features: microvascular proliferation (MVP) and pseudopalisading necrosis (PAN).[18,19] Rather than mere morphological artifacts of rapid growth, we posit that these hypoxic, structurally distinct regions function as 'immunosuppressive sanctuaries.' Within these spatial confines, instead of mere immune evasion, specialized malignant subpopulations actively recruit and reprogram stromal and myeloid partners to erect a physical barrier that selectively excludes cytotoxic effectors while nurturing a pro-tumorigenic microenvironment. Unraveling this spatial "code" requires integrating high-resolution single-cell transcriptomics with spatially resolved multi-omics to map the functional geography of resistance.

To address these challenges, we constructed the Glioblastoma Resistance Insights from Treatment Atlas (GRIT-Atlas), the largest and most comprehensive integrated single-cell transcriptomic resource for IDH-wildtype GBM to date, comprising nearly one million cells from 296 samples. Uniquely, the GRIT-Atlas captures the full spectrum of disease evolution, including primary tumors, recurrences post-standard chemoradiotherapy, and rare cohorts of recurrences following ICB monotherapy and ICB plus anti-angiogenic target combination therapy, stratified by clinical response. By synergizing deep single-cell phenotyping with spatial transcriptomics, we aimed to deconstruct the cellular and spatial logic of therapy-induced evolution.

Here, we report that therapeutic pressure drives a convergent evolution of malignant

cells toward a specific, highly aggressive state: the cNMF7 (MES-like) subpopulation, defined by a synergy of hypoxia, inflammation, and stemness. Crucially, using spatial transcriptomics, we identify the physical reservoir of these cells, defining a "Spatial Resistance Triad" composed of cNMF7 cells, differentiation-arrested E-MDSCs, and Type VI Collagen-secreting myCAFs. We demonstrate that this triad specifically colonizes the hypoxic MVP and PAN niches, where myCAFs act as architects, constructing a fibrotic scaffold via the Collagen/Fibronectin-CD44 axis. This structure not only physically excludes immune effectors but also provides the signaling cues necessary to sustain malignant plasticity and myeloid immunosuppression. Collectively, our findings expose the spatial infrastructure of resistance in GBM, suggesting that overcoming therapeutic failure requires strategies that dismantle this stromal-immune-malignant fortress.

4 Methods

4.1 Human subjects

Patients were prospectively enrolled into this study at First Affiliated Hospital of Soochow University. Written informed consent was provided by all participants according to approved protocol. Fresh tumor tissue was collected at the time of surgery after confirmation of primary glial neoplasm on frozen section. None of the patients was treated with chemotherapy or radiation before tumor resection. Tumors were categorized according to the 2021 WHO Classification of Central Nervous System Tumors based on the combination of relevant histopathologic and molecular features from IHC.

4.2 Treatment-Based IDH-WT GBM Classification

The standard treatment paradigm for IDH-wildtype glioblastoma (GBM), classified as primary GBM (pGBM), involves maximal safe resection followed by radiotherapy with concurrent and adjuvant temozolomide, yet disease recurrence inevitably occurs at a median of 7 months post-diagnosis[20,21]. In current study, recurrent cases segregated into three treatment-defined categories: (1) post-Stupp protocol recurrences (rGBM-R+C); (2) PD-1 inhibitor monotherapy-treated cases (rGBM-ICB), including pembrolizumab (200mg administered 14±5 days pre-resection; Lee et al.[12]) and nivolumab (single preoperative dose; Antunes et al.[14]); and (3) combination therapy cases (rGBM-ICB+Target) featuring PD-1 blockade plus anti-angiogenic agents like anlotinib (12mg daily for 1 week until 2 weeks pre-resection; Mei et al.[13]). Through serial MRI monitoring, we identified responders (demonstrating ≥3 months of tumor stability/regression; n=7) versus non-responders (n=5) in neoadjuvant cohorts, establishing a framework that enables precise molecular characterization of treatment-specific evolutionary patterns and resistance mechanisms in recurrent GBM.

4.3 Single cell RNA library preparation and sequencing

Patient tumors were mechanically cut into about 1-2 mm3 tissue in Dulbecco's modified eagle medium (DMEM) (Gibco). They were then enzymatically digested with the human tumor dissociation kit (Miltenyi Biotec) on the gentleMACS Dissociator (Miltenyi Biotec) per manufacturer instructions. Dissociated cells were filtered by a 70-mm strainer and centrifuged at 300g for 7 min. After removing the supernatant, the pelleted cells were suspended in red blood cell lysis buffer (Miltenyi Biotec) for 2 min to remove red blood cells. The cells were then washed with sorting buffer [phosphate-buffered saline (PBS) supplemented with 2% fetal bovine serum (FBS)] and accessed for viability using trypan blue exclusion. 10,000 - 20,000 cells were loaded for library construction using the 10x Chromium Single cell 5'Library (10x Genomics, V3), according to the manufacturer's instructions. Purified libraries were subject to an Hiseq X Ten sequencer (Illumina) for sequencing with 150-bp paired-end reads.

4.4 Single-cell RNA-seq data preprocessing

Newly generated single-cell sequencing data were aligned with the GRCh38 human reference genome and quantified using Cell Ranger (version 3.0, 10x Genomics). The

preliminary filtered data generated from Cell Ranger were used for downstream filtering and analyses. The quality of cells was then assessed based on two metrics: (1) The number of detected genes per cell; (2) The proportion of mitochondrial gene (Genes starting with 'MT-') counts per cell; (3) The proportion of lysosomal gene (genes starting with 'RPS' or 'RPL') counts per cell; (4) The proportion of hemoglobin gene (genes starting with 'HB' but are not followed by 'P') counts per cell. Specifically, cells with detected genes fewer than 500 or more than 5000, mitochondrial unique molecular identifier (UMI) count percentage larger than 10%, lysosomal UMI count percentage larger than 50%, and hemoglobin UMI count percentage larger than 0.05% were filtered out. To remove the potential doublets, Scrublet[22] was used for each sequencing library with the expected doublet rate set to be 0.05, and cells with the predicted doublet Score larger than 0.3 were further filtered out. Finally, we excluded samples with fewer than 500 retained cells. For scRNA-seq data from other publications, the same filtering steps were applied for the datasets with raw count matrix to obtain high-quality cells. For the specific datasets with no available count data[23-27], the CPM or TPM matrix were downloaded and used directly. However, the subsequent integration process showed that integrating these datasets into the atlas would make it hard to fix the overall batch effect, so these data weren't included in the final atlas. The detailed metadata (including tissue location, sample and patient identifier) were retrieved from the original studies (Table S1).

4.5 Batch effect correction

We next normalized each strictly filtered count data using the *scanpy.normalize_total* function with parameter '*target_sum=1e4*' in Scanpy[28] (v1.10.1). All the normalized data were logarithmically transformed for downstream analyses. The unexpected effects of the total counts and the original identify were regressed out from the normalized expression matrix using the *scanpy.pp.regress_out* function with the parameter setting. Batch effects between samples were preliminarily corrected by simple linear regression. We then used *scanpy.concatenate* function to merge the dataset processed by the unified process together at the data structure level with the parameter '*join = 'inner*''. Batch effects between datasets were preliminarily corrected by merging standardized datasets rather than directly merging count matrices.

For the merged matrices, we scaled each gene to unit variance using sc.pp.scale function with the parameter 'max_value=10', and then highly variable genes (HVGs) were selected using the *scanpy.pp.highly_variable_genes* function with default parameters. Next, principal component analysis (PCA) was performed on the matrix of HVGs to reduce noise and reveal the main axes of variation using the *scanpy.tl.pca* function, and the top 30 components were retained for downstream analyses. The batch effects were corrected by the BBKNN[29] algorithm (v1.6.0), which detected the top nearest neighbors of each cell from each batch respectively instead of the entire cell pool. The parameters of the *scanpy.external.pp.bbknn* function were set to "*batch_key='dataset', n_pcs=30*". As comparison of retaining batch effects, the neighborhood graph was computed using *scanpy.pp.neighbors* function with default parameters following PCA. Finally, Uniform Manifold Approximation and Projection (UMAP) was employed for visualization via the *scanpy.tl.umap* function with default parameters.

4.6 Preliminary annotation

We performed the unsupervised clustering to unveil the structure of IDH-GBM TME population using the *scanpy.tl.leiden* function with the parameter '*resolution=2.0*' and the first round annotation was performed based on the expression of a predefined dictionary of canonical markers, including myeloid cells (*CD14, CD68, FCGR3A, CSF1R, C1QA*), lymphocytes (*CD3D, CD3E, CD8A, NKG7, CD4, CD19*), endothelial cells (*PECAM1, FLT1, ENG, VWF, CLDN5*), stromal cells (*COL1A1, COL1A2, FAP, PDGFRB, ACTA2*), malignant cells (*EGFR, PTPRZ1, METRN, SOX2, NRCAM*), astrocytes/neurons (*GFAP, SLC1A2, NRCAM, TUBB2B, DCX*), and oligodendrocytes (*MBP, PLP1, CLDN11, MOBP, CNP*). The cluster-specific marker genes were identified using the *scanpy.tl.rank_genes_groups* function with the parameter of '*method=t-test*'. 'Express Analysis' module of Metascape[30] (https://metascape.org/gp/index.html) was used to confirming the identification of myeloid cells, lymphocytes, endothelial cells and stroma cells.

Despite oligodendrocytes segregating as an independent cluster, malignant cells remained transcriptionally indistinguishable from neurons and astrocytes when assessed exclusively through canonical marker gene expression. Thus, using non-immune, non-endothelial, and non-stromal cells as input with oligodendrocytes designated as reference normal cells via *infercnvpy.tl.infercnv function with the parameter "reference_cat = "Oligodendrocyte" in Infercnvpy[31] (v0.5.0)*, malignant cells were distinguished from both neurons and astrocytes. The hallmark genomic alterations of GBM[32] - gain of chromosome 7 and loss of chromosome 10 - were utilized as primary classification criteria. However, this approach still failed to resolve transcriptional distinctions between astrocytes and neurons at single-cell resolution.

4.7 Further annotation

For Malignant cells, we performed unsupervised clustering of malignant cells using consensus non-negative matrix factorization (cNMF) implemented in Omicverse[33] (v1.6.10). The malignant cell count matrix was first preprocessed using *omicverse.pp.preprocess* with the parameter "mode='shiftlog|pearson', n_HVGs=2000" to select highly variable genes, followed by scaling (*omicverse.pp.scale*) and principal component analysis (*omicverse.pp.pca*). We then initialized cNMF decomposition using *omicverse.single.cNMF* function with the parameter '*components=np.arange(2,20), n_iter=20, num_highvar_genes=2000*', performing factorization using *omicverse.factorize* function before combining results using *omicverse.combine* function, both with default parameter. To find the optimal number of programs, the *k_selection_plot* function with default parameter was used to calculate the stability and reconstruction error. Finally, consensus clustering was performed using the *omicverse.consensus* function with the parameter 'k=15, density_threshold=0.2'. Programs showing marked overexpression of myeloid, lymphoid, endothelial, stromal, or oligodendrocyte markers and containing relatively few cells were identified as contamination and subsequently excluded from further analysis.

The characterization of non-malignant cells proceeded through sequential classification phases, beginning with lineage assignment using canonical markers: myeloid populations included microglia-derived macrophages (MDMs; *TMEM119, P2RY12, CX3CR1*), bone

marrow-derived macrophages (BMDMs; *CD14, FCGR3A/CD16, CD163, MRC1/CD206*), neutrophils (*S100A8, S100A9, LYZ*), dendritic cells (DCs, *CCR7, CLEC9A, FCER1A*), mast cells (*CPA3, TPSAB1*), and proliferating subsets (*MKI67, TOP2A, PCNA*); lymphoid populations comprised CD4+ T cells (*CD4, IL7R, CD40LG*) including regulatory T cells (*FOXP3, CTLA4, TIGIT, IL2RA, TNFRSF18*), CD8+ T cells (*CD8A, CD8B, GZMK*), B cells (*CD79A, MS4A1/CD20*), plasma cells (*JCHAIN, XBP1, SDC1/CD138*), and natural killer cells (NKs, *NKG7, NCAM1/CD56, FCGR3A/CD16, KLRC1, FGFBP2*); endothelial cells (ECs) were subclassified as arterial (*SEMA3G, EFNB2, GJA4*), venous (*ACKR1, NR2F2, EPHB4*), capillary (*RGCC, CA4, CD36*), and tip-like (*KDR/VEGFR2, ESM1, ANGPT2, CXCR4, PGF*) variants; while stromal components included smooth muscle cells (SMCs, *ACTA2, DES, CNN1, MYH11*), pericytes (PCs, *PDGFRB, CSPG4/NG2, RGS4, ABCC9*), and cancer-associated fibroblasts (CAFs, *FAP, MMP2, COL1A1, PDGFRA, POSTN*).

Subsequent functional refinement primarily relied on differentially expressed genes identified by the *FindAllMarkers* function with default parameter in Seurat[34] (v4.3.0) (Table S2, Table S3), with supplementary evidence drawn from one or more of the following information: (1) pathway enrichment, (2) gene regulatory network inference, or (3) CellChat-mediated cell communication patterns. For instance, the myCAF.01 subpopulation was definitively annotated as 'myCAF.01.COL1' based on its characteristic collagen I signature (COL1A1/COL1A2 upregulation), extracellular matrix pathway activation, and demonstrated COL1A1-CD44 interactions with both E-MDSC and Mal.cNMF7 populations.

4.8 Quantitative Analysis of Cell Cluster Distribution Preferences

Building upon the STARTRAC-dist framework developed by Zhang et al.[35], we implemented a robust quantitative approach to assess cell cluster distribution patterns across treatment groups. Our analytical pipeline calculated the ratio of observed-to-expected cell frequencies ($R_{o/e}$) to precisely quantify cluster-level enrichment or depletion according the following formula:

$$I_{\text{dist}}^{\text{STARTRAC}} = R_{o/e} = \frac{\text{observed}}{\text{expected}}$$

In which expected values were derived from chi-squared test contingency tables comparing cell clusters against treatment groups. This method provides distinct advantages over conventional statistical testing by: (1) generating continuous enrichment scores rather than binary significance thresholds. For example, if $R_{o/e} > 1$, it suggests that cells of the given cell cluster are more frequently observed than random expectations in the specific treatment group, that is, enriched. If Ro/e < 1, it suggests that cells of the given cell cluster are less frequently observed than random expectations in the specific treatment group, that is, depleted; (2) maintaining directional information about cluster redistribution that is lost in traditional chi-squared values, which are defined as $\frac{(\text{observed}-\text{expected})^2}{\text{expected}}$; and (3) enabling cross-comparison of distribution preferences among all cell clusters within our annotated taxonomy.

4.9 Cell Type Benchmarking with Published Signatures

Cell type identification and validation were performed through systematic benchmarking

against established gene signatures from published studies (Table S4). For each cell subpopulation in our atlas, we first identified differentially expressed genes using the *FindMarkers* function in Seurat, followed by selection of the top 100 most significant genes based on statistical metrics. These gene signatures were then compared with published marker sets using Seurat's *AddModuleScore* function to compute enrichment scores for specific cellular states.

For malignant cells, we benchmarked our classifications against four major established frameworks: (1) Ruiz-Moreno et al.'s[36] astrocyte (AC)-like, neural precursor cell (NPC)-like, oligodendrocyte precursor cell (OPC)-like, and mesenchymal (MES)-like states; (2) Neftel et al.'s[24] AC-like, OPC-like, and NPC-like meta-modules with NPC1 and NPC2 subdivisions; (3) Jackson et al.'s[37] T1–T10 malignant cell classification system; and (4) Gavish et al.'s[38] 41 consensus meta-programs representing transcriptional intratumoral heterogeneity patterns across 24 tumor types.

For myeloid populations, we specifically evaluated three functionally characterized subsets: (1) Jackson et al.'s[37] early progenitor myeloid-derived suppressor cells (E-MDSCs) showing upregulation of metabolic and hypoxia pathways located in the pseudopalisading region; (2) Wang et al.'s[39] hypoxia-responsive tumor-associated macrophages (Hypoxia-TAMs) localized in the peri-necrotic niches; and (3) Du et al.'s[40] GPNMB+ MDMs localized in the peri-necrotic areas. (4) Miller et al.'s[41] four consensus immunomodulatory programs, comprising the 'microglial inflammatory' and 'systemic inflammatory' programs, the 'complement immunosuppressive' program (associated with dexamethasone treatment), and the 'scavenger immunosuppressive' program (unique to primary CNS tumors and specifically enriched in hypoxic and vascular niches).

For endothelial cells, we integrated signatures from two high-resolution atlases by Xie et al.: (1) the 2024 atlas[42] distinguishing GBM-EC type 1 (characterized by high vascular permeability and basement membrane remodeling genes like PLVAP and COL4A1) and GBM-EC type 2 (defined by Wnt signaling activation and partial blood-brain barrier retention); and (2) the 2021 atlas[43] delineating distinct anatomical phenotypes, including the quiescent Peripheral EC type I (Pe1) enriched in BBB transporters and the angiogenic, tip-cell-like Tumor Core EC type I (Co1).

For stromal components, we synthesized three complementary classification schemes: (1) Poon et al.'s[15] mesenchymal stromal cell system including astrocytic, fibroblastic, and fibropericytic subtypes; (2) Gao et al.'s[44] cancer-associated fibroblast taxonomy comprising myofibroblastic (myCAF), inflammatory (iCAF), and antigen-presenting (apCAF) fibroblasts; and (3) Du et al.'s[40] recent stromal atlas defining COL6A3+ tumor-associated fibroblasts (TAFs), a specialized matrix fibroblast subset characterized by robust extracellular matrix remodeling signatures and spatial localization within microvascular proliferation (MVP) niches.

4.10 Pathway Enrichment analysis

Pathway enrichment was assessed through two complementary computational approaches to characterize biological processes across cell subpopulations. Pathway activity was inferred using the decoupleR package[45] (v2.9.7) with the PROGENy model, which provides curated pathway-target interactions with regulatory weights for 14 major signaling pathways including Androgen, EGFR, Estrogen, Hypoxia, JAK-STAT, MAPK,

NFkB, p53, PI3K, TGFb, TNFa, Trail, VEGF, and WNT. The analysis utilized the top 500 human pathway-responsive genes ranked by p-value, with normalized log-transformed count matrices processed using the Multivariate Linear Model (mlm) method via the *run_mlm()* function with the parameters ".source = 'source', .target = 'target', .mor = 'weight', minsize = 5". Gene set enrichment analysis (GSEA) was performed on specific cell subpopulations. For each subpopulation, differentially expressed genes were first identified using the *FindMarkers* function in Seurat, followed by selection of the top 100 most significant genes based on statistical metrics. These gene sets were then analyzed using the *GSEA()* function from clusterProfiler[46] (v4.14.6) package with two distinct collections from the Molecular Signatures Database (MSigDB): HALLMARK gene sets (c1.hallmark) and the legacy KEGG pathway collection (c2_kegg_legacy).

4.11 Developmental Potential Quantification Using CytoTRACE 2

To assess cellular developmental potential across our single-cell atlas, we employed CytoTRACE 2[47] (v1.1.0), an interpretable deep learning framework that predicts absolute developmental potential from scRNA-seq data. This validated algorithm classifies cells into discrete potency categories (totipotent, pluripotent, multipotent, oligopotent, unipotent, and differentiated states) while simultaneously generating continuous developmental potential scores ranging from 0 (terminally differentiated) to 1 (totipotent). We applied the *cytotrace2()* function with default parameters to leverage the algorithm's deep neural network architecture trained on diverse developmental datasets to infer developmental potential based on gene expression patterns, where higher CytoTRACE scores (approaching 1) indicate greater developmental plasticity and lower scores reflect lineage commitment.

4.12 Gene Regulatory Network Inference and Transcription Factor Activity Analysis

Gene regulatory network (GRN) inference was performed using the pySCENIC pipeline[48] (v0.12.1). To address data sparsity, we constructed metacells for each subpopulation. Specifically, we performed nearest-neighbor graph construction using the *FindNeighbors* function with parameter "k.param=10", followed by high-resolution clustering using the *FindClusters* function with parameter "resolution=50" to identify metacell groupings. Metacell expression profiles were generated by summing raw counts across all cells within each cluster. Metacells containing fewer than 10 cells were filtered out. The aggregated metacell matrix was further filtered to retain genes expressed in at least 5 metacells and genes present in the hg38 cisTarget database. GRN inference was performed using GRNBoost2 (arboreto_with_multiprocessing.py) and a human TF list derived from motifs-v10nr_clust-nr.hgnc-m0.001-o0.0.tbl. Putative regulons were refined using cis-regulatory motif analysis (pyscenic ctx) against both promoter (hg38_500bp_up_100bp_down_full_tx_v10_clust.genes_vs_motifs.rankings.feather) and extended genomic regions (hg38_10kbp_up_10kbp_down_full_tx_v10_clust.genes_vs_motifs.rankings.feather) databases. Regulon activity scores were calculated for individual cells using the AUCell algorithm implemented via the *ComputeModuleScore* function in Seurat (v4.3.0), with results stored as a new assay for downstream analysis.

4.13 Spatial Transcriptomic Data Collection

Spatial transcriptomic datasets were integrated from five previously published studies representing 48 patient samples profiled using the 10x Visium platform. The studies employed varying sample preservation methods and sequencing strategies: Ravi et al.[49] (n = 16): Fresh frozen IDH-wildtype glioblastoma tissues embedded in OCT compound were sectioned at 10µm thickness. Libraries were prepared using the 10x Visium Spatial Gene Expression kit and sequenced on Illumina NextSeq 550. Mei et al.[13] (n = 16): Fresh frozen GBM tissues were cryosectioned at 10µm thickness and processed using Visium Spatial Gene Expression kits. Libraries were sequenced on Illumina HiSeq X Ten. Ren et al.[50] (n = 3): Fresh frozen GBM tissues were sectioned at 10µm thickness. Libraries were sequenced on both Illumina NovaSeq 6000 (short-read) and Oxford Nanopore PromethION/MinION platforms (long-read). Jackson et al.[37] (n = 2): Formalin-fixed paraffin-embedded (FFPE) glioblastoma tissues were sectioned and processed using the Visium CytAssist Spatial Gene Expression protocol specifically designed for FFPE samples. Libraries were sequenced on Illumina NovaSeq 6000. Greenwald et al.[51] (n = 13): Newly generated spatial transcriptomic data from fresh frozen GBM tissues. Libraries were prepared using standard Visium Spatial Gene Expression protocols and sequenced on Illumina platforms.

All studies utilized the Visium platform but employed distinct sample preservation methods (fresh frozen vs. FFPE) and sequencing technologies, representing the technical diversity in spatial transcriptomic approaches for studying glioblastoma.

4.14 RCTD deconvolution

Cell type deconvolution was performed using Robust Cell Type Decomposition (RCTD) as implemented in the spacexr[52] package (v2.2.0). Comprehensively annotated GRIT-Atlas was employed as reference. For each spatial sample, we created an RCTD object using the *create.RCTD* function. Deconvolution was executed using *run.RCTD* with parameter “doublet_mode = ‘doublet’” to account for potential cell type mixtures within spatial spots. The resulting cell type proportions were incorporated into the spatial Seurat object metadata via the *AddMetaData* function. Cell type weight matrices were systematically extracted and synchronized with corresponding spatial spots, ensuring only common spots between the weight matrix and spatial object were retained for downstream analysis to maintain data integrity.

4.15 MistyR Co-localization inference

Spatial inter-cellular relationships were analyzed using the MISTy framework in the mistyR[53] package (v1.10.0) with a specific focus on identifying cell types that co-localize with the cNMF7 malignant subpopulation. Based on the RCTD deconvolution results, the MISTy framework defined two complementary views for analysis: (1) an *intraview* capturing cell type compositions within each spot, and (2) a *paraview* capturing cellular compositions in the surrounding tissue microenvironment with a radius determined by the mean distance to the nearest neighbor plus one standard deviation. For each of the cell subpopulations in the GRIT-Atlas, we selected the view (intra or para) that provided the strongest explanatory power for spatial relationships as determined by the highest importance values in the MISTy analysis.

The MISTy pipeline was executed independently for each of the 48 spatial samples using the *run_misty* function. For each sample, we extracted the importance values quantifying the spatial relationships between the cNMF7 malignant subpopulation (as predictor) and all other cell subtypes (as targets) from the aggregated results. Results across all samples were systematically compiled to identify consistent spatial relationship patterns between cNMF7 and other cell subtypes in the tumor microenvironment (Table S5).

4.16 Integration and Quantitative Analysis of Recurrent Patterns

To identify recurrent spatial relationship patterns between the cNMF7 malignant subpopulation and other cell types across all 48 samples, we implemented a quantitative thresholding approach. For each cell type, we calculated the frequency of significant spatial associations with cNMF7 across all 48 samples at multiple percentile thresholds (ranging from 10% to 50%). Importance values from MISTy analysis were binarized such that the top n% of values (where n = threshold × 100) were set to 1 and all others to 0, enabling computation of recurrence frequencies for each cell type across the cohort.

The resulting frequency matrices were analyzed using hierarchical clustering with Euclidean distance and complete linkage to identify modules of cell types exhibiting consistent spatial relationship patterns with cNMF7. Since MISTy's importance values indicate the statistical significance of spatial relationships without distinguishing between co-localization (positive association) and mutual exclusion (negative association), we determined the directionality of these relationships through quantitative spatial gradient analysis relative to specific histopathological niches (MVP and PAN), as described below.

4.17 Spatial Association Analysis with microvascular proliferation (MVP) and perinecrotic pseudopalisading (PAN)

To quantitatively analyze spatial relationships between cellular compositions and key histopathological structures in glioblastoma, we employed SPATA2 (v3.1.0), a computational framework specifically designed for spatial transcriptomics data analysis that enables investigation of expression patterns within tissue architecture without prior data grouping. This approach implements the Spatial Gradient Screening algorithm (SAS) as described in Kueckelhaus et al.[54], which facilitates supervised detection of histology-associated expression patterns.

We focused on two hallmark glioblastoma features: microvascular proliferation (MVP) and perinecrotic pseudopalisading (PAN)[18]. Senior neuropathologists identified tissue sections enriched for these features (#UKF259, #UKF260, #UKF275 for MVP; #UKF243, #UKF313, GBM03422 for PAN). Using the *downloadSpataObject* function from the SPATAData package, we obtained pre-processed SPATA2 objects for two representative sections (#UKF275 for MVP, #UKF313 for PAN) following Kueckelhaus et al.'s methodology. Neuropathologists manually annotated the spatial extent of these regions on H&E-stained slides using *createImageAnnotations* function, identifying three distinct pseudopalisading regions surrounding necrotic areas in sample #UKF313 and six MVP regions in sample #UKF275. We then applied the Spatial Gradient Screening algorithm to quantify spatial relationships between cellular proportions (from RCTD deconvolution) and distance to these pathological structures. Distance to annotated regions was calculated using *getCoordsDfSA* function with parameters unit = 'mm' and binwidth = '200um'.

Distance metrics were incorporated as meta-features via *addFeatures* function. Expression gradients of cell type proportions relative to pathological structures were quantified using SAS-specific functions including *plotSasLineplot* function (for linear trends) and *plotSasHeatmap* function (for spatial patterns across distance bins). These spatial gradients allowed us to confirm actual co-localization (increasing proportion with proximity to MVP/PAN) versus mutual exclusion (decreasing proportion with proximity) for the cell modules identified in the recurrent pattern analysis.

4.18 Cell-Cell Communication Analysis

Cell-cell communication analysis was performed using CellChat[55] (v1.6.1), a computational tool that infers intercellular communication networks by integrating single-cell transcriptomic data with a curated database of ligand-receptor interactions. We utilized CellChatDB.human, which contains manually curated literature-supported ligand-receptor interactions, including secreted signaling, extracellular matrix (ECM)-receptor, and cell-cell contact interactions. To investigate specific communication patterns between malignant cells (cNMF7 subtype), cancer-associated fibroblasts (myCAF.02.COL6 and myCAF.03.COL1), and myeloid-derived suppressor cells (E_MDSCs.ADM.HIF), we integrated corresponding subsets from our single-cell atlas and the CellChat pipeline was executed as follows: (1) normalized expression data were input to *createCellChat()* function; (2) over-expressed genes and interactions were identified using *identifyOverExpressedGenes()* function and *identifyOverExpressedInteractions()* function; (3) communication probabilities were computed using *computeCommunProb()* function with the 'triMean' method, followed by pathway-level inference with *computeCommunProbPathway()* function; (4) aggregated networks were calculated using *aggregateNet()* function, and network centrality analysis was performed using *netAnalysis_computeCentrality()* function.

4.19 Meta-Analysis for prognosis and response to ICB

Meta-analysis was conducted with the “meta” package[56]. To reduce inter-cohort heterogeneity, gene expression values were $\log_2$-transformed and standardized into z-scores across patients. Response outcomes were evaluated using risk ratios (RR) by the *metagen* function with the parameter “sm = ‘RR’”, while survival associations were assessed using Benjamini–Hochberg adjusted hazard ratios (HR) by the *metabin* function with the parameter “sm = ‘HR’”, of which the input was derived from univariate Cox regression. Both measures are reported with 95% confidence intervals (CI) based on a random-effects model, and effects were considered statistically significant at $p < 0.05$. Heterogeneity across studies was quantified with Chi-squared tests and I^2 statistics; a p-value below 0.05 accompanied by an I^2 value exceeding 50% was considered indicative of substantial heterogeneity.

4.20 QUANTIFICATION AND STATISTICAL ANALYSIS

All data were analyzed and processed using R (v4.3.2) and Python (v3.10.12), with details of specific functions and libraries provided in the Methods sections. Statistical significance was determined by Mann-Whitney U test (Wilcoxon rank-sum test), Fisher's exact test, Student's t test, Proportion test, Chi-squared test, Pearson Correlation Coefficient, and

Spearman Correlation Coefficient, with a p-value < 0.05 considered statistically significant. Survival comparisons were quantified using log rank Mantel-Cox test and Cox proportional hazards model.

5 Results

5.1 Constructing the GRIT-Atlas: Delineating the TME Landscape Across Therapeutic Modalities

To systematically investigate the cellular and molecular dynamics driving therapeutic resistance in IDH-wildtype GBM, we constructed the GRIT-Atlas, an integrated single-cell transcriptomic atlas comprising 978,065 high-quality cells from 296 GBM samples (Figure 1A, Table S1). This makes the GRIT-Atlas the largest resource of its kind to date. Starting with 22 datasets, we employed a strict, unified quality control (QC) pipeline for all samples with raw count matrices. This pipeline involved filtering cells based on four primary metrics: detected gene counts (retaining cells between 500 and 5,000 genes), mitochondrial (<10%), lysosomal (<50%), and hemoglobin (<0.05%) gene content. Following this, doublet removal was performed using Scrublet. This stringent process led to the ultimate exclusion of five external datasets[23-27] because only available CPM or TPM matrices were provided, which resulted in intractable batch effects during subsequent integration. The final atlas integrates 17 datasets (Figure 1B), including our in-house GusuCohort (n=5) (Figure S1A). Importantly, our atlas captures unique treatment-defined recurrent cohorts: primary GBM (pGBM), post-Stupp protocol recurrences (rGBM-R+C), and two cohorts treated with immunotherapy: PD-1 inhibitor monotherapy (rGBM-ICB) and PD-1 blockade combined with anti-angiogenic agents (rGBM-ICB+T). The rGBM-ICB cohort comprised two external cohorts[12,14] (Antunes et al[14], n=3; Lee et al[12], n=13) and the rGBM-ICB+Target cohort, derived from a single study[13] (n=11), was further stratified based on serial MRI monitoring into Responders (n=7) and Non-responders (n=5), enabling a precise molecular characterization of resistance.

The integration of diverse single-cell transcriptomic datasets, originating from various sources and sequencing platforms, necessitates stringent batch effect correction. We first processed all strictly filtered count data by normalizing the total UMI counts per cell and logarithmically transforming the expression matrix. Subsequently, unexpected technical effects, specifically the total UMI counts and original sample identity, were regressed out using linear regression. After preliminary correction by merging standardized datasets, we performed final batch effect correction using the BBKNN algorithm, focusing on inter-cohort differences as the batch key. Comparison of the integrated UMAP before and after correction demonstrated severe batch effects that resulted in fragmented cell clusters before correction (Figure S1B, left panel). The BBKNN algorithm successfully achieved a highly regularized UMAP with clear delineation of major cell lineages (Figure S1B, right panel). Projection of various metadata, including treatment group, sequencing type (sc/snRNA-seq), sequencing platform, and sample identifier (Figure S1C), confirmed the effective removal of batch variance, providing high confidence for downstream clustering. Initial unsupervised clustering and canonical marker gene expression analysis allowed us to annotate seven major cell lineages (Figure 1C, Figure S1D): Myeloid (349,583 cells; *CD14, CD68, C1QA*), Lymphoid (73,410 cells; *CD3D, CD8A, NKG7*), Endothelial (7,248 cells; *PECAM1, VWF*), Stromal (30,721 cells; *COL1A1, FAP*), Oligodendrocytes (49,238 cells; *MBP, PLP1*), Astrocyte/Neurons (116,308 cells; *GFAP, TUBB2B*), and Malignant cells (367,759 cells; *EGFR, PTPRZ1*).

Consistent with most single-cell studies of glioma, distinguishing malignant cells from normal resident neural cells (Astrocytes and Neurons) based solely on canonical markers proved challenging, as these populations often co-clustered (Figure 1C). To resolve this, we employed inferCNV, utilizing non-immune, non-endothelial, and non-stromal cells as input, with Oligodendrocytes (clusters c15, c34) designated as the reference normal population. Hierarchical clustering based on inferred large-scale CNV profiles successfully segregated Malignant cells (exhibiting hallmark GBM genomic alterations like gain of chromosome 7 and loss of chromosome 10[32]) from normal neural populations (Figure S1E, S1F). The neural/astrocyte clusters (c10, c19, c20, c28, c29) exhibiting CNV profiles similar to the reference oligodendrocyte cluster were identified primarily in snRNA-seq cohorts, consistent with the known preferential detection of neural cells by this technique. Metascape pathway enrichment analysis based on the top 100 marker genes for the Myeloid, Lymphoid, Endothelial, and Stromal compartments strongly supported our initial cell lineage annotations (Figure 1D).

We compared TME composition across treatment groups, excluding all sorted datasets (which necessitates the exclusion of the rGBM-ICB monotherapy cohort from this macro-proportional analysis) (Figure 1E). First, we observed that tumor cell proportion decreased in rGBM-R+C and further decreased in rGBM-ICB+Target samples, consistent with previous reports suggesting lower tumor purity or increased normal tissue content in recurrent surgical specimens[6]. Second, the proportion of normal brain cells (astrocyte/neuron and oligodendrocytes) remained statistically unchanged across the treatment perturbations, with oligodendrocytes showing a non-significant enrichment post-Stupp therapy (rGBM-R+C). Third, for a reliable comparison of the immune compartments, we further restricted the data to whole-cell scRNA-seq samples, excluding snRNA-seq data, as the latter is known to potentially bias against immune cell recovery. This focused analysis revealed that rGBM-R+C samples showed an increase in both myeloid and lymphoid components. Importantly, the addition of ICB+Target therapy further activated the lymphoid compartment while simultaneously reducing the proportion of myeloid cells (the principal immunosuppressive compartment), a finding previously corroborated at the protein level by CyTOF analysis[12]. Finally, we observed a paradoxical non-immune TME remodeling: both endothelial and stromal cells were reduced in rGBM-R+C compared to pGBM. While the aggregate analysis showed a significant proportional increase in both compartments in rGBM-ICB+Target compared to rGBM-R+C, this finding for endothelial cells was counterintuitive given the anti-angiogenic component of the therapy. We therefore performed a cohort-specific comparison to interpret the signal stability (Figure S1G). The endothelial cell proportion was indeed significantly higher in the rGBM-ICB+Target cohort compared to rGBM-R+C (in the scRNA-seq subset), but the magnitude of this difference was minor, and the proportion was statistically indistinguishable from the pGBM (primary) baseline across both scRNA-seq and snRNA-seq cohorts. This non-significant stabilization (or return to baseline) of endothelial cells is consistent with the expected anti-angiogenic effect of the targeted agent clearing pathological vessels, supporting the hypothesis that the initial global increase was primarily a relative enrichment artifact due to reduced malignant cell mass. In sharp contrast, the stromal cell proportion exhibited a highly robust and unique enrichment that persisted significantly in both

aggregate and cohort-specific analyses, particularly in non-responders. This strongly suggested that the stromal component, not the endothelial component, represents the core therapy-resistant microenvironmental shift.

5.2 High-Resolution Dissection of Malignant Cell Subpopulations Identifies Resistance-Associated States

To systematically delineate the transcriptional heterogeneity driving resistance in GBM, we performed unsupervised clustering of the malignant cell compartment using consensus Non-negative Matrix Factorization (cNMF). After rigorous preprocessing, scaling, and PCA, we initialized cNMF decomposition across a range of components (k = 2 to k = 20). The stability and reconstruction error were calculated to determine the optimal. We observed that while reconstruction error consistently decreased, the stability fluctuated; however, k = 15 yielded a high stability score and the largest separation between stability and reconstruction error (Figure S2A), indicating optimal fidelity. Thus, 15 transcriptional programs were identified (Figure S2B). Four programs—cNMF9 (Stromal), cNMF13 (Myeloid), cNMF14 (Oligodendrocyte), and cNMF15 (Lymphoid)—were subsequently excluded based on marked overexpression of non-malignant lineage markers, consistent with potential cellular contamination (Figure S2C, D). The final analysis yielded 11 distinct functional states of malignant cells (Figure 2A, B), confirming effective batch effect removal (Figure S2E).

We annotated these 11 programs through systematic benchmarking against established GBM malignant cell classification frameworks, including the canonical AC-like, OPC-like, NPC-like, and MES-like states from prior study[24] (Figure S2F, Table S2, Table S3, Table S4). The majority of our programs aligned with these established states: cNMF8 was characterized by a potent proliferating signature (*MKI67, TOP2A, CENPF, CCNB1, AURKB*) coupled with significant MAPK pathway activation; cNMF1 was identified as OPC-like (*PDGFRA, OLIG1, BCAN, PMP2, FABP7*); cNMF5 as AC-like (*ATP5B, ATP5A1, COX4I1, COX5B, CYCS*); and cNMF4/11 as NPC-like (*SOX4, SOX11, DCX, ELAVL4, MYT1L*) (Figure S2G). Intriguingly, we identified a less emphasized functional state comprising cNMF6, cNMF10, and cNMF12, which exhibited a strong Neuron-like (NEU) signature (*SYT1, GRIA4, CACNA1C, NRXN3, DLG2*). While initial consideration focused on potential neuronal contamination, these three programs consistently displayed high activity in the p53 and PI3K signaling pathways (Figure 2C, D)—signatures highly inconsistent with terminally differentiated, quiescent neurons. Moreover, these cells were retained after preliminary filtering via inferCNV, providing further evidence against their benign origin. We therefore rigorously classify these as a malignant NEU-like state, which is highly poised to mediate tumor-neuron interactions. Although NEU-like GBM cells typically constitute only a small fraction of the total tumor population, their biological significance is increasingly recognized in GBM invasion and recurrence. This is consistent with spatial analyses suggesting that NEU-like cell abundance increases with distance from the tumor core, often co-existing with normal neurons and astrocytes in the infiltrating brain parenchyma[16]. This malignant NEU-like state thus warrants focused investigation due to its potential role in driving disease spread[57-59].

Program cNMF7 was confirmed as the canonical MES-like state (Figure 2D). It exhibited an extreme signature of Hypoxia and robust activation of key immunoregulatory and pro-tumorigenic pathways, including TNFA, TGFB, and NFKB, alongside high activity in immune response (JAK-STAT), proliferation (MAPK), and angiogenesis (EGFR, VEGF). This program was characterized by high expression of markers associated with

inflammation (*CHI3L1, MIF, SERPINE1*), invasion (*SPP1, VIM, FN1*), hypoxia (*VEGFA, ADM, EPAS1*), anti-apoptosis (*MCL1, SOD2, HSPB1*), metabolic reprogramming (*NAMPT, PGK1, HLPDA*), stemness (*CD44, ID1, ANXA1*), and stress (*FOS, JUN, ATF3*) (Figure S2H). Gene Regulatory Network (GRN) inference identified a shared core of transcription factors (TFs)—BHLHE41, CEBPD, CEBPB, MSX1, IRF3, XBP1, EGR1, KLF6, CTCF—with high activity common to cNMF7, cNMF1, and cNMF5. Uniquely, cNMF7 exhibited distinct high activity for ELF3, NFIL3, and BHLHE40 (Figure 2E, Table S2).

We next investigated the effect of therapeutic pressure on malignant cell state distribution (excluding sorted cohorts). Compared to primary GBM (pGBM), standard Stupp protocol recurrence (rGBM-R+C) showed a significant increase in the proportions of all three Neuron-like programs (cNMF6, cNMF10, cNMF12) and two MES-like programs (cNMF2, cNMF3) (Figure 2F, G). Critically, under the pressure of ICB plus targeted combination therapy (rGBM-ICB+Target), the highly metabolic AC-like (cNMF5), highly invasive classic MES-like (cNMF7), and highly proliferative cNMF8 programs were overwhelmingly enriched, collectively accounting for over 80% of malignant cells in this cohort (Figure 2H). This substantial shift indicates that combination therapy imposes strong selective pressure, dramatically reshaping the GBM cellular landscape and prioritizing these core resistance features. Furthermore, cNMF7 was found to be almost exclusively restricted to the non-responder subset of the combination therapy cohort, underscoring its pivotal role in treatment resistance and immune evasion. To evaluate stemness and proliferative potential, CytoTRACE 2 analysis showed that cNMF8 had the highest developmental potential, followed closely by cNMF7 (Figure 2I). While SOX2 and NES were broadly expressed, the classic surface stem cell marker PROM1/CD133 was largely absent. Notably, CD44 was found to be specifically and highly expressed in cNMF7 (Figure 2J). Although cNMF7 exhibited relatively low proliferative activity, an ssGSEA score derived from its top 100 markers accurately identified patients with the poorest prognosis across seven independent GBM cohorts (Figure S2I). This suggests that the highest risk is driven not by the most proliferative cells, but by the highly plastic, stem-like cNMF7 "silent killer".

In summary, high-resolution cNMF analysis of malignant cells not only precisely resolved canonical GBM subtypes but, crucially, identified cNMF7 (classic MES-like state) as the core resistance subpopulation robustly selected under combination therapy pressure. This state is defined by a unique transcriptional regulatory network and high expression of the stemness marker CD44, providing a mechanistic link to poor clinical outcome and highlighting its role as a key driver of therapeutic resistance.

5.3 Treatment Pressure Selects for Immunosuppressive Myeloid Subpopulations Associated with ICB Resistance

Myeloid cells represent the most abundant immune population within the GBM TME and are essential regulators of immune suppression and therapeutic resistance. Initial coarse-grained annotation of the myeloid compartment (Figure 3A, Figure S3A) identified six major populations: Microglias (MGs; 54.4%), Bone Marrow-derived Macrophages (BMDMs; 37.1%), Neutrophils (3.7%), Dendritic Cells (DCs; 2.0%), Proliferating Myeloid Subsets (2.6%), and Mast Cells (0.2%) (Figure 3B). We investigated the impact of therapeutic interventions on the proportional representation of the four most abundant myeloid classes (MGs, BMDMs, Neutrophils, and DCs) within the total immune compartment (Figure 3C, upper panel). Standard chemoradiotherapy (rGBM-R+C) did not induce significant proportional changes across these four classes. Conversely, Immunotherapy (ICB) or combination therapy (ICB+Target) was associated with a trend of decreased MG proportion and a reciprocal increase in the BMDM proportion, consistent with published observations, linking these shifts to GBM malignant cell MES transformation[6,14]. Notably, DCs showed significantly higher proportions in both the ICB monotherapy and ICB+Target cohorts compared to pGBM or rGBM-R+C groups, suggesting DC activation is a key feature of the post-ICB TME. Neutrophils were significantly elevated only in the ICB+Target combination group (Figure 3C, lower panel). Proliferating myeloid cells were reduced post-ICB monotherapy, in accordance with prior research[6], but exhibited an increase in the ICB+Target group relative to ICB monotherapy, suggesting the anti-angiogenic component of the combination therapy may exert a modulatory effect on myeloid proliferation (Figure S3B). Mast cells were too rare (detected in only 2 pGBM and 1 ICB+Target sample) for meaningful analysis.

Following robust batch correction (Figure S3C), we performed high-resolution subclustering on the four major myeloid classes, resolving a total of 23 distinct myeloid subpopulations (Figure 3A, Table S2, Table S3), including 5 MG, 7 BMDM, 5 Neutrophil, and 6 DC subsets. Functional annotation revealed diverse transcriptional programs: Within the MG compartment, we identified a pro-inflammatory subset (MG.01.CXCL2.NFKB1), a neuroprotective/resting state (MG.02.PARK2), an immediate-early gene activation state (MG.03.CCL3.EGR.JUN), an S100 family expressing subset (MG.04.TXNIP.S100A), and a Type I IFN response subset (MG.05.CXCL10.IFI). The BMDM subsets included IFN-stimulated states (BMDM.01.ISG.CXCL9), lipid metabolism subsets (BMDM.02.APOE), a high ribosomal protein subset (TAM.03.RPL), and a TGFβ signaling subset (BMDM.04.TGFB1). Crucially, the BMDM lineage yielded three key immunosuppressive populations: the intermediate monocyte subset (Mono.CD14.FCGR3A), the early progenitor MDSC (E-MDSC) subset (E_MDSCs.ADM.HIF), and the monocytic MDSC (M-MDSC) subset (M_MDSCs.CXCL1.CXCL2.CXCL3.FCN1.IL10). Neutrophil subsets included NFKB-active (Neu.01.NFKB1), antigen presentation/stress (Neu.02.HLA_DRB5), IFN-I response (Neu.03.CXCL10.IFI), metabolically active (Neu.04.ATP5), and a PMN-MDSC-like population (PMN_MDSCs.FCGR3B). Finally, the DC compartment comprised canonical cDC1 (cDC1.01/02.IRF8), cDC2 (cDC2.SIRPA.ITGAX), the mature/T-cell activating DC3 (DC3.LAMP3.CCR7), pDC (pDC.NRP1), and moDC (moDC.CLEC10A) subsets (Figure 3D).

Functional analysis of these 23 subsets revealed several critical associations with therapeutic response (Figure 3E, F, G). First, we identified six distinct subsets across all four lineages with elevated JAK-STAT pathway activity (Neu.03.CXCL10.IFI, BMDM.01.ISG.CXCL9, MG.05.CXCL10.IFI, cDC1.02.IRF8, DC3.LAMP3.CCR7, and Mono.CD14.FCGR3A). With the exception of Mono.CD14.FCGR3A, all five were robustly enriched post-ICB/ICB+Target, suggesting that IFN-mediated JAK-STAT signaling is the primary mechanism of myeloid activation by immunotherapy. Crucially, the Mono.CD14.FCGR3A subset was almost exclusively present in and significantly enriched within non-responders of the ICB+Target cohort. Defined as "intermediate monocytes" ($CD14^{high}CD16/FCGR3A^{high}$), this population has been previously linked to dysfunctional and immunosuppressive phenotypes in glioma patients[60,61]. Our pathway enrichment analysis revealed that, alongside IFN-related JAK-STAT signaling, this subset uniquely exhibited high activation of Oxidative Stress, Complement Activation, and Epithelial-Mesenchymal Transition (EMT) pathways (Figure S3D). These functional signatures delineate Mono.CD14.FCGR3A as a key resistance population that is activated by therapy but simultaneously endowed with potent suppressive machinery. Furthermore, all DC subtypes were enriched in post-ICB samples, suggesting DCs are important functional targets of ICB. However, while five DC subtypes correlated with higher response rates, the DC3.LAMP3.CCR7 subset was significantly enriched in ICB+Target Non-responders. The enrichment of DC3.LAMP3.CCR7, the canonical mature and migratory DC subset, in non-responders is counter-intuitive and suggests a functional re-programming toward an immunosuppressive state. Supporting this, pan-cancer analyses have defined LAMP3+DCs as a terminal maturation state potentially linked to immune tolerance and characterized by high expression of immunosuppressive markers[62]. We posit that this subset is hijacked by the overwhelming suppressive cues present in the non-responder TME, failing to prime anti-tumor T cells and instead promoting T-cell exhaustion or tolerance. However, evidence suggests that DCs are indeed activated by therapy: Lee et al.[12] showed that DCs in recurrent tumors following standard treatment exhibited upregulation of genes associated with Type I IFN (*IFI6, IFI27*) and NFκB (*NFKB1*) pathways compared to newly diagnosed tumors. This suggests that while DCs may be activated by treatment, their extremely limited numbers may lead to suboptimal intratumoral antigen presentation, resulting in insufficient T cell anti-tumor activity. This implies that further promoting intratumoral DC activation or trafficking might be a potential strategy to achieve a more sustained response to neo-aPD1. We observed a clear dichotomy in lineage enrichment related to response: nearly all MG and Neutrophil subsets (excluding Neu.04.ATP5) were enriched in ICB+Target Responders, whereas virtually all BMDM/Monocyte subsets (TAM.01-04, Mono.CD14.FCGR3A, E/M-MDSC) were enriched in non-responders. This strong segregation supports the notion that MG and Neutrophils should be collectively categorized as pro-inflammatory myeloid components, while BMDMs and their monocyte progenitors form the core immunosuppressive component. Finally, benchmarking against established immune programs[41] revealed that both MG and BMDM exhibited high activity in the Complement Immunosuppressive Program, with MG further expressing the Microglial Inflammatory Program and BMDM expressing the Scavenger Immunosuppressive Program. We made the novel finding that Neutrophils and DCs

displayed significantly higher activity in the Systemic Inflammatory Program, which was not a focus of the previous study, highlighting the significant pro-inflammatory and anti-tumor potential of these two lineages (Figure S3E).

The consensus in the field and our proportional analysis suggest that immune suppression is primarily driven by BMDMs, which are derived from peripheral monocytes (Mono) and immature myeloid cells (IMCs) infiltrating the TME[5]. These progenitors differentiate into mature macrophages (BMDM.01-04) or, due to maturation arrest, into Myeloid-Derived Suppressor Cells (MDSCs) (E-MDSC and M-MDSC). CytoTRACE analysis strongly supported this developmental hierarchy (Figure 3H), showing that the Mono subset was the only population with relatively high differentiation potential, while all other myeloid subsets (both mature BMDM and arrested MDSC) exhibited uniformly low differentiation potential. Consistent with MDSC identity, the E-MDSC and M-MDSC populations displayed restricted maturation (low CD14, CD16/FCGR3A), low expression of antigen presentation genes (e.g., HLA-DRB1, CD74), and distinct expression profiles from classic M2-like markers (e.g., CD163, MRC1) (Figure 3I). To further validate the MDSC identity, we benchmarked our BMDM/MDSC subsets against three previously reported hypoxia-associated myeloid programs: Jackson et al.'s E-MDSCs[37], Wang et al.'s Hypoxia-TAMs[39], and Du et al.'s GPNMB+ MDMs[40] (Table S4). Calculation of the respective scores (Figure 3J) confirmed the high specificity of our subsets: the Jackson et al. E-MDSC score and the Du et al. GPNMB+ MDM score were both highest in our E-MDSC.ADM.HIF subset, while the Wang et al. Hypoxia-TAM score was highest in both the E-MDSC.ADM.HIF and M_MDSCs.CXCL1.CXCL2.CXCL3.FCN1.IL10. Given that E-MDSC and M-MDSC were the only BMDM/MDSC populations observed in our study to exhibit a profound hypoxic signature (driven by genes like ADM and HIF-1α), the consistent overlap in scores across all three published gene sets strongly suggests that the Hypoxia-TAMs and GPNMB+ MDMs identified in those studies are functionally and transcriptionally equivalent to the MDSCs (E/M-MDSC) we have characterized.

In summary, high-resolution myeloid analysis precisely defined two functionally opposed myeloid camps: the pro-inflammatory MG/Neutrophil axis enriched in responders, and the immunosuppressive BMDM/MDSC axis enriched in non-responders. We identified the Mono.CD14.FCGR3A subset as a therapy-activated, highly suppressive hallmark of resistance and validated that E-MDSC and M-MDSC represent the core, hypoxic bone marrow-derived immunosuppressive cell population in the GBM TME.

5.4 Heterogeneous Lymphoid Responses: The Dual Roles of T Cells and NK Cells

The lymphoid compartment, though often little and functionally impaired within the GBM TME, plays a critical role in mediating anti-tumor immunity. Our initial coarse-grained annotation of the lymphoid cells identified six major populations (Figure 4A, Figure S4A, S4B): CD4+ T cells (26.7%; *CD4, IL7R, CD40LG*), including regulatory T cells (Tregs; *FOXP3, CTLA4, TIGIT, IL2RA, TNFRSF18*); CD8+ T cells (42.0%; *CD8A, CD8B, GZMK*); B/Plasma cells (4.9%; *CD79A, MS4A1/CD20, JCHAIN, XBP1, SDC1/CD138*); Natural Killer cells (NKs; 13.0%; *NKG7, NCAM1/CD56, FCGR3A/CD16, KLRC1, FGFBP2*); Stress T cells (6.0%); and Proliferating T cells (4.4%), and gamma delta T cells (3.0%) (Figure 4B). We next assessed the impact of therapeutic intervention on the proportional representation of the four major lymphoid classes (CD4+ T, CD8+ T, B/Plasma, NK) within the total immune compartment (Figure S4C). Consistent with the myeloid compartment, standard chemoradiotherapy induced no significant proportional changes in any of the four major lymphoid classes. Conversely, both CD8+ T and NK cells showed a significant proportional increase following ICB monotherapy, with a further upward trend observed in the ICB+Target group. CD4+ T cells did not exhibit this strong proportional increase. B/Plasma cell proportions were significantly elevated only in the ICB+Target combination therapy group, showing no marked change after ICB monotherapy.

After confirming the effective correction of batch effects (Figure S4D), we performed high-resolution subclustering on the four major lymphoid classes, resulting in 36 distinct subpopulations (Figure 4C, Table S2, Table S3): 9 CD4+ T subsets (including 2 Treg subsets), 13 CD8+ T subsets (7 Cytotoxic T Lymphocyte/Exhausted (CTL/Tex), 6 Naïve/Memory), 7 B/Plasma subsets (4 B, 3 Plasma), and 7 NK subsets. The NK subsets were further defined by both CD16, NCAM1/CD56 and the inhibitory receptor NKG2A/KLRC1[63] (Figure S4E), yielding 4 $CD16^{high}$ $NKG2A^{low}$, 2 $CD16^{low}$ $NKG2A^{high}$, and 1 $CD56^{high}$ $NKG2A^{high}$ $CD16^{low}$ subset. In our T cell analysis, we accurately identified naïve cells (*CCR7, SELL, TCF7*) based on mRNA expression. However, we note that the distinction between memory and helper T cell subsets was difficult to reliably annotate due to low expression or minor inter-subset variation of established markers. Therefore, results concerning these memory/helper T cell annotations should be interpreted with caution. Crucially, in contrast to some previous GBM T cell transcriptomic studies[64], our atlas definitively captured a population of terminally Tex marked by classical markers (*PDCD1, HAVCR2, LAG3, TIGIT, CTLA4*). However, the transcriptional boundary between CTL and Tex subsets was often blurred, as cytotoxic indicators (*IFNG, GZMB*) were not mutually exclusive across clusters. This supports the classic model where CTLs gradually transition into Tex states under chronic antigenic stimulation[65].

We then focused on the functional characteristics and treatment perturbations across these 36 subsets (Figure 4D, 4E, 4F, S4F). PC and GC subsets, indicative of Tertiary Lymphoid Structures (TLS), showed an increased proportion post-immunotherapy (ICB and ICB+Target). However, they were predominantly enriched in the non-responders following ICB+Target therapy. This aligns with recent findings that TLS in adult gliomas exhibit functional heterogeneity: while B:T-TLS and PC-TLS are mature immune hubs associated with improved survival, T-low-TLS lack effective immune cell infiltration,

accumulate malignant cells, and exhibit high proportions of immunosuppressive CD163+ macrophages, potentially acting as "immature" or "non-functional" suppressive structures[66]. Our data suggest that even when TLS are present (as indicated by the increase in PC/GC subsets), their functional heterogeneity may be a key factor driving resistance to immunotherapy. Complementing this resistance profile, both Treg subtypes exhibited a consistent proportional increase across standard treatment, ICB monotherapy, and ICB+Target combination therapy, and were preferentially enriched in non-responders, consistent with established findings[13]. Treg.01 (Classic Treg; *FOXP3, CTLA4, TNFRSF18, TIGIT*) showed high activity in Hypoxia, NFκB, TGFβ, and VEGF pathways. Treg.02 (a novel Treg subset; *HLA-DRB1, LGALS1, UCP2, ISG15, S100A4*) displayed high activation of TNFα, JAK-STAT, EGFR, and WNT pathways. The high Hypoxia activity in both subsets suggests that Tregs are actively maintained within the tumor's hypoxic, immune-privileged niches.

Conversely, the proportion of CTLs increased following both standard and immunotherapy, with a further rise after ICB+Target therapy. Notably, all 3 CTL subsets were enriched in responders, supporting extensive literature linking the expansion of cytotoxic CD8+ T cells to ICB efficacy[12,67]. While Tex proportions also slightly increased post-immunotherapy (consistent with increased checkpoint sexpression in recurrent tumors post-nivolumab[6,12,13]), their enrichment pattern was highly divergent: only the Tex.03.ALDOA.MIF subset (*ALDOA, ZFP36, DUSP2, MIF, VIM*), which exhibited the most profound hypoxic signature among all lymphoid cells, was enriched in non-responders. This subset likely represents the truly dysfunctional T cell state arrested by the TME's overwhelming suppressive cues, particularly hypoxia. Conversely, other Tex subsets, including the highly exhausted Tex.02.Terminal (*HAVCR2, LAG3, TIGIT, CTLA4, CXCL13, VCAM1*), showed enrichment in responders. This critical finding suggests that ICB (especially in combination) may partially reverse the epigenetic and transcriptional exhaustion program in certain Tex populations, potentially rendering them as "reinvigoratable" Tex precursor cells that still contribute to anti-tumor activity. Treatment caused no obvious proportional perturbation to total Memory and Naïve T cells, though specific subset proportions were affected. We also observed a significant increase in Stress T and gamma delta T cell proportions post-ICB+Target therapy, whereas Proliferating T cells showed no significant difference across treatment groups. Finally, NK cells also showed significant perturbations: the NKG2A^{high}CD16^{low} and CD16^{high}NKG2A^{low} subsets both exhibited a marked proportional increase, particularly following ICB+Target intervention. The NKG2A high CD56^{high} CD16^{low} subset, despite being proportionally higher in untreated GBM, was not significantly perturbed by therapy but was identified by CytoTrace 2 as the population with the highest differentiation potential (Figure 4G), suggesting it serves as the progenitor pool for the two increasing NK subsets. Further analysis revealed that NK subsets displayed response-dependent enrichment: for instance, one NKG2A^{high} CD16^{low} subset (NKG2AhiCD16lo.01.ZNF683) was enriched in responders, while another (NKG2AhiCD16lo.02.ISG15) was enriched in non-responders. This suggests complexity in the NK-mediated anti-tumor immune process within the TME. While Mathewson et al. have revealed the suppressive role of NK cell receptors (such as CD161) on T cell anti-tumor function[23], and we did not observe any CD8+ T cell subset

exhibiting significantly high NK-like transcriptional features, we still found that the NK compartment exhibited significantly higher expression of cytotoxic programs compared to the T cell compartment (Figure 4H, Table S4), once again emphasizing the essential, yet often overlooked, role of NK cells in mediating anti-tumor immune responses in GBM.

High-resolution analysis of the lymphoid compartment revealed a complex picture of treatment-induced shifts defined by a critical response-resistance dichotomy. Efficacy is characterized by the enrichment of CTLs and "reinvigoratable" Tex precursors, alongside an expansion of NK subsets. Conversely, resistance is marked by the specific accumulation of the hypoxic, dysfunctional Tex.03.ALDOA.MIF and a proportional increase of the immunosuppressive Treg subsets. The enrichment of B/Plasma cells in non-responders suggests that treatment-induced lymphoid aggregation may manifest as dysfunctional TLS, further contributing to the suppressive TME. This data underscores that therapeutic success requires not only the activation of effector cells but the selective depletion or functional redirection of specific, highly suppressive Treg and Tex subtypes.

5.5 Treatment-Driven Plasticity: Identifying Resistance-Associated Endothelial and Stromal Subpopulations

The Endothelial Cells (ECs, 26.0%) and Stromal Cells (74.0%) constitute another critical compartment of the GBM TME. Initial coarse-grained annotation (Figure 5A, B) subclassified ECs into arterial (*SEMA3G, EFNB2, GJA4*), venous (*ACKR1, NR2F2, EPHB4*), capillary (*RGCC, CA4, CD36*), and tip-like (*KDR/VEGFR2, ESM1, ANGPT2, CXCR4, PGF*) variants (Figure S5A), and stromal components into smooth muscle cells (SMCs, *ACTA2, DES, CNN1, MYH11*), pericytes (PCs, *PDGFRB, CSPG4/NG2, RGS4, ABCC9*), and cancer-associated fibroblasts (CAFs, *FAP, MMP2, COL1A1, PDGFRA, POSTN*) (Figure S5B). To focus on treatment-induced changes, we performed proportional analysis between the primary (pGBM), standard recurrent (rGBM-R+C), and combination recurrent (rGBM-ICB+Target) cohorts, excluding CD45+ sorted samples due to potential non-representativeness of the mixed EC/Stromal fractions. Crucially, the proportion of the CAF lineage was significantly elevated in the rGBM-ICB+Target group compared to both pGBM and rGBM-R+C (Figure S5C), a trend confirmed in Mei et al. 's cohort (Figure S5D). This proportional increase in the CAF compartment under the pressure of combination therapy, despite the anti-angiogenic component, suggests a robust, adaptive fibrotic response that warrants immediate scrutiny, whereas other cell type proportions remained relatively stable.

Following effective batch correction (Figure S5E, F), high-resolution subclustering resolved the stromal and EC compartments into 18 distinct subsets: 10 EC and 8 Stromal subsets (Figure 5A, B, C, Table S2, Table S3). The 8 Stromal subsets included five CAF, two PC subsets, and one SMC subset. The CAF lineage was segmented into three myCAF subsets—myCAF.01.POSTN.MMP11 (involved in matrix remodeling, marked by genes including *POSTN, COL12A1, MMP11*), myCAF.02.COL6 (involved in matrix stiffening, mainly defined by Type VI Collagen genes *COL6A1* and *COL6A2*), and myCAF.03.COL1 (collagen-producing, marked by genes including *COL1A1* and *COL1A2*). Additionally, we identified apCAF.CD74, which exhibits antigen presentation characteristics (*CD74, HLA-DRB1*), and the highly proliferative prolCAF.TOP2A (*TOP2A, MKI67*). The two pericyte subsets were PC.01.RGS5 and PC.02.PDGFRB, and the single smooth muscle cell subset was SMC.ACTA2.MYH11. The 10 endothelial cell subsets included two arterial EC subsets (Arterial.01.DKK2 and Arterial.02.CXCL12), five capillary EC subsets (Cap.01.RGCC (metabolism-associated), Cap.02.CA4 (blood-brain barrier-associated, marked by genes including *CA4, CLDN5*), Cap.03.PDGFRB (pericyte interaction-associated), Cap.04.MKI67 (proliferative), and Cap.05.SPP1 (inflammatory type)), two tip-like EC subsets (Tip_like.01.PGF.CXCR4 and Tip_like.02.ANGPT2), and one venous EC subset (Vein.VCAM1).

Functional and proportional analysis (Figure 5D, E, F) highlighted the paradoxical and highly heterogeneous angiogenesis observed under combination therapy. Despite the pressure exerted by anti-angiogenic targeted therapy, two EC subsets, Vein.VCAM1 and Arterial.01.DKK2, showed increasing proportional trends and were consistently enriched in non-responders. Both exhibited high activity in the EGFR, NFKB, and VEGF pathways, alongside JAK-STAT activation, indicating they are immune-resistant nascent vascular structures regulated by immune signals. Comparative benchmarking against published

glioma EC studies by Xie et al.[42,43] (Figure 5G). suggests that Arterial.01.DKK2 may correspond to the peripherally located Pe2 subtype, characterized by high antigen-presenting features; while the Vein.VCAM1 subset shares a similar immuno-inflammatory phenotype (high VCAM1 and inflammation-related gene expression) with the Co3 (tumor core) or Inflammatory EC subtypes. This strongly suggests that under combination therapy pressure, the tumor evolves compensatory, resistant neovascular networks in different regions: Pe2-like cells (Arterial.01.DKK2) may promote peripheral immune evasion by enhancing immune activation signals, and Co3/Inflammatory EC-like cells (Vein.VCAM1) may mediate core inflammatory responses via high VCAM1 expression. Together, they act as critical microenvironmental nodes driving therapeutic failure through JAK-STAT-mediated immune interference. Furthermore, our study identified two Tip-like subsets with distinct phenotypes and prognoses, revealing the high heterogeneity and plasticity of the glioma vasculature under diverse therapeutic pressures: the Tip_like.01.PGF.CXCR4 subset displayed high EGFR, VEGF, and TGF-β signaling activity, and its molecular features were highly similar to the Angiogenic Tip (Co1) or TEC Type 1 subtypes, representing active and stressed nascent vascular tips. This subset was predominantly enriched in samples recurring after Target + ICB combination therapy, suggesting these cells initiate robust angiogenesis and repair mechanisms that form the basis of tumor resistance and recurrence. In contrast, the Tip_like.02.ANGPT2 subset was characterized by high p53, MAPK, and PI3K pathway activity, was enriched in samples recurring after standard treatment, and dominated in Target + ICB non-responders. This phenotype may align more closely with the stress-tolerant, dysfunctional TEC Type 2 subtype. This distinction indicates that the increase in the Tip_like.01.PGF.CXCR4 subset reflects adaptive resistance to Target + ICB, while the persistent presence of the Tip_like.02.ANGPT2 subset may reflect inherent resistance of standard-treatment-residual vascular structures to subsequent combination therapy, underscoring the necessity of designing heterogeneous therapeutic strategies that target specific vascular subsets.

Stromal cell analysis provided critical context for TME remodeling. Our CAF subsets were consistent with the classic classification of antigen-presenting (apCAF), inflammatory (iCAF), and myofibroblast-like (myCAF) subtypes (Figure 5H, Table S4). We found that the apCAF.CD74 subset concurrently exhibited antigen-presenting features (high HLA molecules) and significant inflammatory characteristics (high TNFA, VEGF activity), with JAK-STAT activation hinting at potential perturbation by immunotherapy. The three myCAF groups we identified consistently showed strong Hypoxia and TGF-β pathway activity, suggesting their core role in fibrosis and matrix remodeling. The most crucial finding was the significant upregulation of the Type VI Collagen-secreting myCAF.02.COL6 subset after targeted combination immunotherapy, with even greater enrichment in non-responders. The molecular and functional characteristics of this subset highly align with the role of the COL6A3+ CAF (where COL6A3 encodes Type VI Collagen) focused on by Du et al.[40] in enhancing vascular fibrosis and mediating combination therapy resistance. Notably, both apCAF.CD74 and myCAF.02.COL6 showed significant upregulation after targeted combination immunotherapy and higher enrichment in non-responders, indicating they are key microenvironmental components driving therapeutic failure. In contrast, myCAF.01 and myCAF.03 were reduced in number after targeted combination immunotherapy, with

myCAF.01 showing little association with therapeutic response, while myCAF.03 was predominantly associated with Responders, suggesting complexity and spatial specificity in the ECM regulatory network. This finding aligns with the concept identified by Poon et al. that PDGFRB+ mesenchymal stem cells (MSC) in the MVP region can differentiate into various perivascular stromal cells (PVSCs), including CAFs, pericytes, and smooth muscle cells, potentially contributing to MVP formation[15]. Compared to this finding, our myCAF subset, characterized by Type I and VI collagen secretion, exhibited high transcriptional similarity to both the less differentiated MSC and the fibroblastic subtype MSC identified in their study. Consistent with this progenitor-like identity, our CytoTRACE 2 analysis indicated that the CAF lineage possessed greater differentiation potential than PC and SMC, with the Type VI Collagen-secreting myCAF.02 subset showing the strongest differentiation potential (Figure 5I), even exceeding the highly proliferative prolCAF. Collectively, this analysis suggests that regardless of specific nomenclature, this highly plastic, hypoxic, and resistance-associated CAF population—exemplified by myCAF.02.COL6—may be selectively maintained as functionally activated progenitor cells under therapeutic pressure, playing a critical role in forming the GBM immunosuppressive and fibrotic microenvironment.

In summary, targeted combination immunotherapy (ICB+Target) selects for specific stromal and endothelial resistance phenotypes. The myCAF.02.COL6 subset, defined by Type VI Collagen secretion and heightened differentiation potential, was significantly upregulated and highly enriched in non-responders, suggesting it drives resistance via enhanced vascular fibrosis and niche support. Simultaneously, immune-resistant neovascular EC subsets (Vein.VCAM1 and Arterial.01.DKK2) accumulated in non-responders, characterized by active EGFR, NFKB, and JAK-STAT signaling. These findings reveal that therapeutic failure results from the synergistic establishment of treatment-refractory fibrotic and neovascular networks maintained by myCAF.02.COL6 and specific EC populations.

5.6 Spatial Transcriptomic Profiling Reveals a cNMF7-Centric Niche within Hallmark Hypoxic Regions of Glioblastoma

To systematically characterize the spatial organization of the TME components relative to the aggressive malignant cNMF7 subpopulation, we integrated and analyzed spatial transcriptomic data from 48 GBM patient sections, leveraging diverse published datasets[13,37,49-51]. Following cell type deconvolution using RCTD, we employed the MISTy framework to quantify the spatial relationships (co-localization or mutual exclusion) between the cNMF7 cells and all other identified cell subtypes of the GRIT-Atlas. This quantitative integration approach, which included calculating the recurrence frequency of significant spatial associations, identified five distinct modules of cell types based on their consistent spatial relationship patterns with cNMF7. Module 1 (4 subsets), Module 2 (8 subsets), and Module 3 (14 subsets) exhibited the strongest recurrent spatial associations with cNMF7, while the remaining subsets were distributed in Module 4 (22 subsets) and Module 5 (24 subsets) (Figure 6A, Figure S6A, Table S5). Given the striking hypoxic signature of the cNMF7 subpopulation, and the strong consensus that two hallmark histopathological features—microvascular proliferation (MVP) and perinecrotic pseudopalisading (PAN)—are associated with severe hypoxia[18], we hypothesized that the cNMF7 cells and their strongly associated Module 1-3 partners collectively define a core hypoxic niche located within the MVP and PAN regions.

To test this hypothesis, we first focused on the MVP feature. We selected sample #UKF275 (Ravi *et al.*) as a representative section containing prominent MVP regions (Figure 6B). Senior neuropathologists manually delineated six MVP regions on the H&E-stained slides (Figure 6B), which allowed us to generate spatial gradients of cellular composition relative to the annotated regions. Consistent with the prevailing literature and our hypothesis, the MVP region in this section was confirmed to be the most severely hypoxic area, as demonstrated by the hypoxia gene signature enrichment (Figure 6C). Subsequently, we quantified the proportions of the 26 cell subsets within Modules 1–3 relative to the distance from the MVP regions (Figure S6B). We observed that the highest proportions of cNMF7, E-MDSC.ADM.HIF1A, myCAF.02.COL6, and prolCAF.MKI67 were precisely localized within the MVP area, with their proportions dropping sharply as the distance from the MVP region increased (Figure 6D, E, F). Importantly, this robust co-localization pattern was independently validated in two additional MVP-containing sections, #UKF259 and #UKF260 (Figure 6G, H).

Next, we investigated the PAN feature. We utilized sample #UKF313 (Ravi *et al.*) as a representative section encompassing PAN regions (Figure 6I). Based on previous expert annotations[54], the section featured three necrotic areas surrounded by pseudopalisading cells (Figure 6I). We noted that the necrotic cores exhibited significantly reduced sequencing read counts. Crucially, the PAN regions surrounding these cores were confirmed to be the most hypoxic areas in the section (Figure 6J), aligning with established GBM pathology and our underlying assumption. Analysis of the spatial gradients (Figure S6C) revealed that the highest proportions of cNMF7, E-MDSC.ADM.HIF1A, myCAF.02.COL6, and myCAF.02.COL1 were concentrated within the PAN area (Figure 6K, L, M). The proportion gradients showed an initial brief increase immediately adjacent to the necrotic core (due to the low count detection within the core itself) followed by a gradual

decline as the distance increased. This specific co-localization signature was also consistently observed in two other PAN-containing sections, #UKF243 and GBM03422 (Figure 6N, O).

In summary, the combined spatial transcriptomic analysis of 48 patient samples reveals a highly recurrent, spatially organized compartment within hallmark GBM structures. The aggressive malignant cNMF7 subpopulation forms the core of this niche, consistently co-localizing with E-MDSC.ADM.HIF1A, and specific subsets of CAFs (myCAF.02.COL6 and myCAF.02.COL1/prolCAF.MKI67) specifically in the severely hypoxic MVP and PAN regions.

5.7 Key Communication Axes: Collagen/Fibronectin-CD44 Drive myCAF Crosstalk with cNMF7 and E-MDSC

The malignant cNMF7 subpopulation is characterized as a classic MES-like cell type, consistent with the previously identified T4 cells (Jackson *et al.*). Similarly, our E-MDSC.ADM.HIF1A subset aligns with previously reported highly hypoxic myeloid populations, including Hypoxia-TAMs (Wang *et al.*[39]), GPNMB+MDMs (Du *et al.*[40]), and hypoxic E-MDSCs (Jackson *et al.*[37]), in which the co-localization and potential interaction between MES-like tumor cells and E-MDSCs in the hypoxic niche have been extensively studied. Our integrated spatial transcriptomic analysis (Figure 6) established high-hypoxia myCAFs as an essential third compartment of this niche. While the co-localization of general CAF populations and MES-like tumor cells in regions corresponding to sample #UKF275 (Ravi *et al.*) has been previously reported[68], our findings precisely map this spatial relationship to the histopathological hallmarks of MVP and PAN and identify the functional CAF subtype as extracellular matrix (ECM)-secreting myCAFs. Therefore, this section is dedicated to dissecting the critical intercellular communication axes between myCAFs, cNMF7 malignant cells, and E-MDSCs within this tripartite hypoxic niche.

CAFs are widely recognized as multifaceted regulators of the TME, critically influencing progression through both the extensive deposition of the ECM and active signaling transduction (e.g., promoting immunosuppression and metabolic support)[69,70]. Our analysis of ECM-related communication pathways revealed two highly significant myCAF-initiated interactions (Figure 7A). First, myCAF-derived Collagen I and Collagen VI were predicted to engage the CD44 receptor expressed on both MES-like tumor cells and E-MDSCs. Second, myCAF-secreted Fibronectin (FN1) was also predicted to engage the same CD44 receptor on these malignant and immune cell subsets. Given that the Integrin family is classically considered the primary receptor for Collagens and Fibronectin[71], we specifically investigated the probabilities of these ligand-receptor pairs and consistently identified CD44 as the strongest potential communication recipient for both Collagen and FN1 (Figure 7B). This is highly relevant as Migliozzi *et al.* previously demonstrated a critical role for the membrane receptor CD44, mediated by Collagen and Fibronectin signaling, in the Glycolytic/Plurimetabolic (GPM) cell archetype aggregation[16]. While they identified the enrichment of these interactions within the GPM archetype, our data definitively establish the myCAF functional subtype as the source of these signaling-competent ECM ligands and precisely map this communication axis to the MVP and PAN hypoxic niches.

In addition to ECM, myCAFs utilize soluble factors (Figure S6D). Specifically, myCAFs potentially communicate with E-MDSCs via the secretion of Macrophage Migration Inhibitory Factor (MIF), which is inferred to engage the multi-receptor complex of CD74/CXCR4/CD44 on the E-MDSC surface. Furthermore, myCAFs appear to signal to MES-like tumor cells through the secretion of Pleiotrophin (PTN), which interacts with Nucleolin (NCL) on the tumor cell surface. In the context of direct cell-to-cell communication (Figure S6E), the Collagen VI-secreting myCAF subset is suggested to interact with cNMF7/E-MDSCs via homophilic CD99 interaction, and also with E-MDSCs via the myCAF surface molecule APP binding to E-MDSC-expressed CD74. The observed expression patterns of these ligands and receptors across the four cell types align with these predicted interactions (Figure 7C). Spatially, the ECM-related ligand-receptor pairs

show specific high expression within both MVP (Figure 7D) and PAN (Figure 7E) regions, supporting our inference. Conversely, while MIF showed region-specific high expression in both MVP and PAN areas, its inferred receptors (CXCR4/CD74) did not exhibit evident high expression (Figure S6F). This observation—where a key soluble ligand is highly expressed but its primary receptors are not co-localized—suggests a structural inefficiency or a non-canonical mode of signaling for the MIF axis, contrasting with the high-fidelity co-localization observed for the core Collagen/FN-CD44 axis.

The reciprocal regulation of myCAFs by E-MDSCs and cNMF7 cells is equally crucial. In soluble factor-mediated communication (Figure 7F), E-MDSCs primarily signal to myCAFs by secreting Secreted Phosphoprotein 1 (SPP1), which is predicted to interact with various Integrin receptors and CD44 on the myCAF surface. Concurrently, MES-like tumor cells signal through the secretion of PTN, engaging NCL/SDC2 receptors on myCAFs. Given that MES-like cells acquire ECM-secreting capabilities through mesenchymal transition, we also analyzed their ECM-related communication (Figure S6G). Here, cNMF7 cells were found to signal to myCAFs by secreting Tenascin C (TNC), Laminin-β1 (LAMB1), and FN1, which engage myCAF-expressed Integrin receptors. Direct cell-to-cell contact interactions were limited to the aforementioned homophilic CD99 binding (Figure S6H). The cellular expression profiles of these ligands and receptors validate the plausibility of these inferred interactions (Figure 7G).

Spatially, the SPP1 ligand and its cognate receptors (CD44, ITGAV+ITGB1, ITGA5+ITGB1) showed specific high expression in the MVP region (Figure 7H), although ITGAV itself was highly expressed ubiquitously across the section. However, neither SPP1 nor its receptors (with the exception of CD44) showed significant region-specific high expression in the PAN area (Figure 7I). Furthermore, the TNC/PTN ligands also exhibited specific high expression in the MVP region, with their receptors NCL/SDC2 showing a corresponding, albeit less specific, elevation. This spatial co-localization of the TNC/PTN signaling axes was also not significantly observed in the PAN region (Figure S6I). These findings reinforce the notion of distinct signaling environments within the two histopathological hypoxic niches, with the SPP1 and TNC/PTN axes being particularly active in MVP.

Collectively, these results delineate a highly organized and reciprocal communication network centered around the myCAF-driven ECM. The key Collagen/Fibronectin-CD44 axis acts as a foundational, high-fidelity signaling conduit established by myCAFs, linking them directly to the malignant cNMF7 cells and the immunosuppressive E-MDSCs. This tripartite interaction, spatially confined to the hypoxic MVP and PAN regions, establishes a complex microenvironmental shield that promotes mesenchymal state maintenance, physical barrier formation, and myeloid cell suppression. Furthermore, the observed heterogeneity in signaling pathways (e.g., SPP1 and PTN axes) between MVP and PAN suggests that while the core resistance triad is conserved, the precise regulatory mechanisms deployed are niche-specific, necessitating tailored therapeutic intervention strategies.

5.8 Clinical Relevance and Pan-Cancer Validity of the myCAF-ECM-CD44 Axis

To translate our mechanistic findings into a clinical context, we hypothesized that the myCAF-driven secretion of COL1, COL6, and FN1—which we identified as the core ligands engaging CD44 on mesenchymal-like glioma stem cells—serves as a robust biomarker for patient outcome and therapeutic resistance. To substantiate this, we conducted a comprehensive bulk transcriptomic and proteomic interrogation of the six identified key CD44 ligands (*COL1A1, COL1A2, COL6A1, COL6A2, COL6A3, FN1*).

Building upon these spatial and intercellular inferences, we hypothesized that the myCAF-driven secretion of COL1, COL6, and FN1 constitutes a critical axis engaging CD44 on mesenchymal-like glioma stem cells to sustain the immunosuppressive niche. To substantiate this prior to experimental validation, we conducted a comprehensive bulk transcriptomic and proteomic interrogation of six key CD44 ligands (*COL1A1, COL1A2, COL6A1, COL6A2, COL6A3, FN1*). In the GRIT-Atlas, collagen expression was restricted to stromal cells, while *FN1* was abundant in both stromal and endothelial compartments. Conversely, *CD44* expression was ubiquitous, peaking in lymphoid and myeloid lineages but remaining detectable across neural, endothelial, and stromal populations (Figure S7A). Analysis of our in-house bulk RNA-seq cohort confirmed that mRNA levels of all six ligands were significantly upregulated in tumor tissue compared to normal brain and exhibited a positive correlation with tumor grade (Figure S7B). Survival analysis across seven independent GBM cohorts revealed that elevated expression of these ECM components consistently stratified patients with poor prognosis. Notably, while *COL6A2* and *COL6A3* did not reach statistical significance, they maintained a clear hazard trend (Figure S7C). Furthermore, regarding therapeutic efficacy, high expression of all six ligands was uniformly associated with a lower objective response rate to immunotherapy, although statistical significance was exclusively reached by *COL6A2* (Figure S7D).

Leveraging the Ivy Glioblastoma Atlas Project[18], we validated the spatial fidelity of our findings: all six ligands exhibited peak expression in peri-vascular regions and secondary enrichment in peri-necrotic zones, rigorously corresponding to the MVP and PAN niches identified in our spatial transcriptomic analysis (Figure S7E). Correlation analysis further cemented the link between this ECM module and the immunosuppressive microenvironment. Expression of the six ligands correlated positively with markers of M2-like TAMs, Tregs, and MDSCs, and T-cell exhaustion, while showing strong positive associations with angiogenesis, EMT, and hypoxia signatures (Figure S7F).

Finally, extending our scope to a pan-cancer perspective using TCGA data, we observed that these ECM ligands correlate with poor prognosis in over two-thirds of cancer types (Figure S7G). Proteomic validation via CPTAC and GTEx datasets demonstrated that while these ECM proteins are upregulated in most tumors—with kidney renal clear cell carcinoma (RCC) and GBM showing universal overexpression—heterogeneity exists, suggesting that while the pro-tumorigenic role of this ECM axis is broadly applicable, its magnitude is context-dependent.

6 Discussion

The failure of immune checkpoint blockade (ICB) in phase III clinical trials for GBM underscores a critical gap in our understanding of how the TME evolves under therapeutic pressure. While intrinsic tumor heterogeneity is a known hurdle, the spatial reorganization of the ecosystem driving treatment resistance has remained elusive. Here, we present the GRIT-Atlas, the most comprehensive single-cell landscape of IDH-wildtype GBM to date, covering the full spectrum of disease evolution from diagnosis to recurrence following standard-of-care (SOC) and combinatorial immunotherapy. Beyond cataloging cell states, our study identifies a convergent evolutionary trajectory where therapeutic stress selects for a specific mesenchymal-like malignant state (cNMF7). Crucially, utilizing spatial transcriptomics, we define a "Spatial Resistance Triad"—comprising cNMF7, hypoxic E-MDSCs, and Type VI Collagen-secreting myCAFs—that physically fortifies the immune-privileged niches of MVP and PAN. This spatial sanctuary, maintained by the ECM-CD44 axis, represents a formidable barrier to T cell-mediated cytotoxicity and highlights the necessity of dismantling the stromal architecture to sensitize GBM to immunotherapy.

GBM recurrence is driven by the remarkable plasticity of malignant cells. Our cNMF analysis reveals that while SOC pressure enriches for Neuron-like states—potentially exploiting synaptic integration for survival—the addition of ICB and anti-angiogenic therapy drives a dramatic shift toward the cNMF7 (MES-like) state in non-responders, which is defined by a specific convergence of stemness (CD44+), profound hypoxia, and inflammatory signaling (NFκB/TNF). This suggests that the "MES" subtype described in bulk genomics is not a monolithic entity but rather a heterogeneous compartment where cNMF7 represents the ultimate stress-adaptive, drug-tolerant persister state. The exclusive enrichment of cNMF7 in non-responders implies that therapeutic strategies must move beyond broad anti-tumor agents to specifically target the upstream regulators (e.g., *ELF3, BHLHE40*) that lock cells in this lethal phenotype.

A major controversy in neuro-oncology revolves around the identity of immunosuppressive myeloid cells: are they M2-polarized macrophages or distinct developmental states? Our high-resolution mapping resolves this by distinguishing E-MDSCs from canonical M2-like TAMs. We demonstrate that the hypoxic, immunosuppressive populations previously identified as "Hypoxia-TAMs" (Wang *et al.*), "GPNMB+ MDMs" (Du *et al.*), or "E-MDSCs" (Jackson *et al.*) are transcriptionally convergent and likely represent the same functional entity: differentiation-arrested, bone marrow-derived E-MDSCs. Our data argue against a simple M1-to-M2 polarization model. Instead, we propose a "maturation arrest" model, where hypoxic niches within the TME prevents monocyte-to-macrophage differentiation, locking cells in a potent, enduring immunosuppressive E-MDSC state. Consequently, therapeutic efforts should shift from trying to "re-polarize" M2 macrophages to inducing the differentiation or elimination of these E-MDSCs, potentially by targeting their specific survival cues (e.g., MIF or CD44 signaling) within the hypoxic niche.

The most significant conceptual advance of our study is the spatial definition and mechanistic elucidation of the resistance niche. Previous work has alluded to these spatial relationships, yet with conflicting definitions of the myeloid and stromal components.

Specifically, two earlier studies reported on the spatial relationship involving CAFs, malignant cells, and immune components. Jain *et al.*[68] demonstrated the co-localization of CAFs with mesenchymal glioblastoma stem cells (GSCs), endothelial cells, and M2 macrophages in the representative UK275 section; our observation that myCAFs co-localize with MES-like malignant cells and inhibitory myeloid cells in the MVP area aligns with their findings also in the representative UK275 section. In contrast, Du *et al.*[40], analyzing neoadjuvant immunotherapy data, proposed a distinct mechanism: COL6A3+CAFs, typically situated in the MVP area, secrete TGF β3/CSF1 to reprogram macrophages into GPNMB+ immunosuppressive subtypes (which we identify as E-MDSCs) found in the PAN area, an interaction which ultimately fosters T cell exclusion via GPNMB-ITGB5. Furthermore, Poon *et al.*[15] utilized Digital Spatial Profiling (DSP) of the perivascular region and identified vascular/perivascular stromal cells (PVSCs)—which our trajectory analysis links to a high-differentiation-potential myCAF subset—co-localizing with HLA-DRA^{low} inhibitory monocytes and resident perivascular macrophages. Although this study did not focus on tumor cells, the distribution of tumor stem cells in the microenvironment around blood vessels has been widely recognized[72]. These studies establish a consensus on the importance of the CAF-GSC-Myeloid axis in MVP or PAN region, but diverge on the specific identity (M2 vs. E-MDSC) and the precise spatial compartmentalization of the interaction.

Our findings integrate and refine these perspectives. We support the model of CAF co-localization with MES-like glioblastoma stem cells and immunosuppressive myeloid cells in the MVP/PAN regions, similar to our observations. We identify myCAF.02.COL6 as the specific stromal architect, which is linked to the PVSC population and actively constructs a physical and signaling scaffold in MVP/PAN regions. This subset promotes the structural enforcement of the E-MDSC state and cNMF7 stemness via the high-fidelity Collagen/Fibronectin-CD44 axis, establishing an impermeable microenvironmental shield that physically excludes T cells. Crucially, while our study identifies the central immunosuppressive myeloid cell in this core resistance niche as E-MDSC, this focused view does not negate the extensive body of evidence showing CAF-mediated crosstalk with M2 macrophages or their polarization potential. Rather, our focus is on a specific, spatially-defined cellular interaction centered on the stress-adapted, mesenchymal-like malignant core within the most restrictive pathological zones (MVP/PAN).

Our spatial intercellular communication analysis identifies Type I Collagen (*COL1A1, COL1A2*), Type VI Collagen (*COL6A1, COL6A2, COL6A3*), and Fibronectin (*FN1*) as ECM components specifically enriched in the MVP and PAN niches. We posit that their interaction with CD44, the receptor highly expressed on recipient cells in these regions—constitutes a critical regulatory axis driving immunosuppression and therapeutic resistance. CD44, a non-kinase single-pass transmembrane glycoprotein upregulated in aggressive cancer cell subsets, serves as a canonical molecular marker for cancer stem cells (CSCs). It functions as a versatile receptor for diverse ECM ligands, including hyaluronan (HA), osteopontin (OPN), chondroitin, collagens, fibronectin, and so on, and orchestrates multiple signaling pathways fundamental to cancer biology[73]. In glioma, CD44 is established as a GSC marker[74] and is significantly upregulated in perivascular and peri-necrotic zones[75]. Despite its recognition as a receptor for collagens and fibronectin, current

understanding of CD44-COL/FN interactions is largely confined to spatial co-localization[76], structural biology[77], and *in vitro* blocking studies[78], underscoring the high value of investigating its functional role within the TME. Beyond CD44, the ligands themselves are implicated in glioma progression. *COL6A1* expression correlates with higher tumor grade and poor prognosis, showing significant enrichment around necrosis[79]. *COL6A3* protein is enriched in the GBM core, particularly in perivascular regions, and co-localizes with the stemness marker NES[80]. CAF-derived FN1 has been shown to induce GBM cell migration and invasion[81]. Furthermore, while fibroblasts are the canonical source, ECM secretion is also acquired by tumor cells[82], mesenchymal stem cells[83], and endothelial cells[84] undergoing mesenchymal transition, a state characterized by enhanced proliferation, invasion, and ECM production. Although direct evidence of physical binding and downstream mechanisms for the Collagen/Fibronectin-CD44 axis in GBM remains nascent, a recent study demonstrated a parallel mechanism where CAF-secreted COL1 interacts with CD133 to upregulate *SLC1A5*, thereby promoting GSC tumorigenesis[85]. Consequently, elucidating this specific axis represents the central priority for our subsequent investigation.

A further complexity involves the spatial organization of malignant cells. Migliozzi *et al.*'s high-resolution CosMx imaging data demonstrated that malignant cell subtypes, including the GPM subtype (corresponding to our MES-like cells), exist in both clustered (structural, often in PAN/MVP) and dispersed (plastic) spatial patterns. The clustered GPM cells, which maintain their cell identity, are found in distinct regions (PAN and non-PAN clusters), while dispersed GPM cells exhibit unique microenvironmental interactions[16]. Given that our spatial approach is intrinsically focused on the distinct, aggregated pathological structures of MVP and PAN, our conclusions primarily capture the biology of these clustered resistance niches and their reciprocal interactions. This means our study may underrepresent the unique cell-cell communication dynamics occurring with the more dispersed, invasive tumor and immune cell states.

Our study should be interpreted within the context of several methodological and intrinsic biological limitations. First, the statistical power to definitively attribute cellular shifts to combination therapy is challenged by two factors: Sample Size and Stochasticity and Cell Sorting Bias. While our total cell count is massive, the number of patients in the key rGBM-ICB+Target subgroup is relatively small. This raises concerns about the influence of inter-patient heterogeneity and stochastic factors on the observed cell state enrichments. To mitigate this, we utilized the large, unsorted NatCancer (Mei 2023) cohort—which spans primary, SOC recurrence, and combination therapy groups—specifically as an independent validation cohort to exclude the influence of accidental factors (stochasticity). Furthermore, some cohorts incorporated cell sorting (CD45+ or CD3+ selection), inherently distorting native TME proportions. Consequently, we excluded sorted samples from macro-level TME proportion analyses; nevertheless, absolute comparisons of immune cell ratios remain challenging. Second, we observed a significant Sequencing Technology Bias (specifically, snRNA-seq versus scRNA-seq), which necessitates careful interpretation when comparing specific cell types and states. Due to the inherent nature of nuclear isolation, snRNA-seq exhibits a higher propensity to capture neuronal lineage cells. Specifically, we found that cohorts employing snRNA-seq showed a significantly higher

proportion of Oligodendrocytes, suggesting a potential overestimation bias for this lineage; however, Astrocytes and Neurons did not display a strong sequencing technology dependency (Figure 1). Crucially, even after rigorous cross-dataset batch correction, a subtle residual batch effect related to sequencing method (sc/sn) persisted for specific myeloid cell states. Myeloid cells originating from snRNA-seq samples showed a propensity to cluster into specific subtypes (Microglia favored MG.02.PARK2, and BMDM favored TAM04.TGFB1), an effect not observed in other cell types (Figure S3). This suggests that the two methods possess differential sensitivity for capturing distinct cell states (rather than broad cell types). Therefore, future comparisons involving these specific glial and myeloid states must be approached with caution, potentially requiring separate analyses of snRNA-seq and scRNA-seq datasets to ensure robust conclusions. Third, we must consider the significant influence of Intra-tumoral Spatial Heterogeneity on cell type quantification. The cellular composition and proportions of the tumor microenvironment (TME) are known to vary substantially across different pathological sampling regions within a single tumor, specifically between the tumor core, the enhancing rim, and the tumor-infiltrating zone. Although the inclusion of a massive number of samples (n=296 GBM samples) partially mitigates the overall impact of this variability on general cell type composition, its influence on the interpretation of subtle proportional differences and specific cell state enrichments still warrants cautious consideration. Fourth, reliance on cross-sectional data precludes the definitive assertion of causality; our observations describe associations rather than proving that cNMF7 cells "evolved" from a pre-existing state in the same patient through treatment pressure, necessitating future lineage-tracing studies in paired longitudinal samples.

The identification of the Spatial Resistance Triad (cNMF7 + E-MDSC + myCAF) fundamentally shifts the therapeutic paradigm for recurrent GBM. Targeting T cells via PD-1/PD-L1 blockade alone is insufficient because the T cells are physically and functionally excluded from these core resistance niches. Effective therapy likely requires a multi-pronged approach: (1) Dismantling the Scaffold: Targeting myCAFs or the Collagen-CD44 axis to disrupt the physical niche; (2) Relieving Hypoxia: Optimizing anti-angiogenic dosing to normalize vessels without inducing the severe hypoxia that fuels E-MDSCs and cNMF7; and (3) Myeloid Reprogramming: Differentiation therapy to unlock the arrested E-MDSC state. The GRIT-Atlas provides the blueprint for designing such rational combinatorial strategies to breach the fortress of GBM resistance.

7 Legends

7.1 Figure Legend

Figure 1. Construction and single-cell landscape of the GRIT-Atlas in IDH-wildtype glioblastoma. (A) Schematic workflow illustrating the study design, including data collection from 17 cohorts, rigorous quality control (QC), treatment-based stratification, and integration into the final UMAP embedding. **(B)** Detailed characterization of the integrated datasets, displaying cell type composition, treatment groups, cell and sample counts, FACS sorting status, and sequencing modality (scRNA-seq vs. snRNA-seq) for each cohort. **(C)** Dot plot visualizing the expression of canonical marker genes across seven major cell lineages. Dot size reflects the percentage of expressing cells, and color intensity represents average expression levels. **(D)** Bar plots showing the top 5 enriched pathways (Metascape) for the top 100 signature genes identified in lymphoid, myeloid, stromal, and endothelial cell populations. **(E)** Comparative analysis of cell type proportions across primary (pGBM), standard-of-care recurrent (rGBM-R+C), and ICB plus anti-angiogenic recurrent (rGBM-ICB+Target) tumors. The upper panel includes all data, while the lower panel is restricted to scRNA-seq data to mitigate technical bias from nuclear sequencing. Statistical significance was determined by the Wilcoxon rank-sum test. **See also Figure S1.**

Figure 2. Identification of therapy-driven malignant states and evolutionary trajectories in GBM. (A) UMAP visualization of malignant cells derived from all cohorts, colored by the 11 consensus Non-negative Matrix Factorization (cNMF) programs (meta-programs). **(B)** Feature plots illustrating the spatial distribution and usage intensity of distinct cNMF programs on the UMAP embedding. **(C)** Heatmap showing the activity of 14 signaling pathways quantified by DecoupleR for each cNMF program. **(D)** Dot plot displaying the expression of top marker genes defining each malignant state. Dot size indicates the percentage of expressing cells, and color represents average expression. **(E)** Circular heatmap visualizing the regulatory network activity. Each ring corresponds to one of the 11 cNMF programs, showing the activity of the top 10 regulons (transcription factors) identified by pySCENIC. **(F and G)** Tracking clonal evolution across therapeutic modalities. **(F)** Alluvial plot depicting the proportional shifts of cNMF states from primary tumors (pGBM) to recurrences after standard-of-care (rGBM-R+C) and combinatorial immunotherapy (rGBM-ICB+Target). **(G)** Corresponding Ratio of Observed to Expected (Ro/e) heatmap quantifying the enrichment preference of each cNMF state within the three treatment groups. **(H)** Pie charts comparing the composition of malignant states between non-responders (top) and responders (bottom) specifically within the rGBM-ICB+Target cohort. **(I)** Differentiation potential analysis using CytoTRACE2. Left: UMAP colored by predicted differentiation score (high score indicates high stemness). Right: Box plots quantifying the developmental potential across different malignant clusters. **(J)** Feature plots visualizing the expression of canonical stemness markers (*SOX2*, *NES*, *PROM1*, *CD44*) versus proliferation markers (*MKI67*, *PCNA*, *TOP2A*, *CENPF*). **See also Figure S2.**

Figure 3. Hierarchy, functional heterogeneity, and therapy-induced remodeling of the myeloid compartment. (A) High-resolution UMAP visualization of the myeloid landscape. Center: Global embedding showing major lineages, including Microglia (MG), Bone

Marrow-Derived Macrophages (BMDM), Dendritic cells (DC), Neutrophils, Mast cells, and Proliferating cells). Corners: Detailed sub-clustering of MG (top-left), DCs (top-right), BMDMs (bottom-left), and Neutrophils (bottom-right). **(B)** Nested donut charts illustrating the hierarchical composition of myeloid cells. The inner ring represents the proportion of each major lineage within the total myeloid compartment, while the outer ring details the composition of sub-clusters within each lineage. **(C)** Box plots quantifying the abundance of major myeloid lineages (normalized to CD45+ cells) across primary GBM (pGBM), standard-of-care recurrence (rGBM-R+C), ICB recurrence (rGBM-ICB), and combinatorial recurrence (rGBM-ICB+Target). Statistical significance was determined by the Wilcoxon rank-sum test. **(D)** Heatmap displaying the expression of top marker genes distinguishing each fine-grained myeloid subtype. **(E)** Pathway activity analysis using DecoupleR. The heatmap shows the activation scores of 14 biological pathways across myeloid subtypes. **(F)** Alluvial plot tracking the dynamic shifts in myeloid subpopulation proportions across the four clinical stages: pGBM, rGBM-R+C, rGBM-ICB, and rGBM-ICB+Target. **(G)** Ratio of Observed to Expected (Ro/e) heatmap, aligned with **(F)**, quantifying the enrichment or depletion preference of each subtype within the distinct treatment groups. **(H)** Differentiation potential analysis using CytoTRACE2. Top: UMAP colored by predicted differentiation score. Bottom: Box plots showing the distribution of developmental potential scores across clusters, indicating lineage plasticity. **(I)** Dot plot characterizing BMDM phenotypic states based on the expression of classical monocyte (*CD14*, *CD16*), M2-like (*MRC1*, *CD163*, *TGFB1*), and antigen-presentation (*HLA-DRB1*, *HLA-DRA*, *CD74*) markers. **(J)** Kernel density estimation of immunosuppressive signatures using Nebulosa to recover gene expression signals. The plots visualize the weighted density of gene sets defining E-MDSCs (Jackson et al.), Hypoxia-TAMs (Wang et al.), and GPNMB+ MDMs (Du et al.) projected onto the BMDM UMAP embedding. **See also Figure S3.**

Figure 4. Divergent functional states and treatment-associated dynamics of T and NK lymphocytes. (A) UMAP visualization showing the fine-grained sub-clustering of four major lymphoid lineages: CD4+ T cells, CD8+ Memory/Naïve T cells (Tm/Tn), CD8+ Cytotoxic/Exhausted T cells (CTL/Tex), and Natural Killer (NK) cells. **(B)** Nested donut charts displaying the hierarchical composition of each lymphoid lineage. The inner ring represents the proportion of the lineage within the total lymphoid compartment, while the outer ring details the distribution of its specific subsets. **(C)** Heatmaps illustrating the expression of distinct marker genes defining the sub-clusters for each lineage, corresponding to the order in **(A)**. **(D)** Pathway activity landscape. The heatmap shows DecoupleR-inferred activity scores for 14 signaling pathways across the identified lymphoid subsets. **(E)** Alluvial plot tracking the proportional shifts of lymphoid subpopulations across primary tumors (pGBM) and recurrences following standard-of-care (rGBM-R+C), ICB monotherapy (rGBM-ICB), and combinatorial immunotherapy (rGBM-ICB+Target). **(F)** Ratio of Observed to Expected (Ro/e) heatmap, aligned with **(E)**, quantifying the enrichment preference of lymphoid subsets within each treatment group. **(G)** Differentiation potential of NK cells inferred by CytoTRACE2, projected onto the NK sub-cluster UMAP. **(H)** Heatmap comparing the functional strength of Cytotoxicity (*PRF1, GZMB, GZMA, GZMH, NKG7, GNLY*) and NK cell (*KLRD1, FGFBP2, FCGR3A, S1PR5, KLRC1, KLRC3, KLRB1, KLRC2*) signatures between CD8+ CTL/Tex and NK cell populations. Scores were

calculated using AUCell. **See also Figure S4.**

Figure 5. Remodeling of the perivascular and stromal niche under therapeutic pressure. (A) Detailed landscape of the non-immune stromal compartment. **Center:** Integrated UMAP visualization distinguishing Endothelial cells (left cluster) from Stromal cells (right cluster). **Inner Flanks:** Feature plots displaying canonical markers for Endothelial cells (*VWF, PECAM1, FLT1*) and Stromal cells (*ACTA2, TAGLN, COL1A1*). **Outer Flanks:** Independent sub-clustering UMAPs showing the fine-grained heterogeneity of Endothelial (far left) and Stromal (far right) populations. **(B)** Nested donut charts illustrating the hierarchical composition of Endothelial (top) and Stromal (bottom) lineages. Inner rings represent major lineage proportions, while outer rings detail subtype distributions. **(C)** Heatmaps characterizing the distinct transcriptional profiles of Endothelial (left) and Stromal (right) sub-clusters using top marker genes. **(D)** Pathway activity analysis inferred by DecoupleR, highlighting functional heterogeneity across stromal and endothelial subsets. **(E)** Alluvial plot depicting the dynamic shifts in cell state proportions across primary (pGBM), standard-of-care recurrent (rGBM-R+C), and combinatorial immunotherapy recurrent (rGBM-ICB+Target) tumors. **(F)** Ratio of Observed to Expected (Ro/e) heatmap, aligned with **(E)**, quantifying the enrichment patterns of each subset across the three treatment groups. **(G)** Differentiation potential of Stromal cells analyzed by CytoTRACE2. **Top:** UMAP colored by predicted stemness score. **Bottom:** Box plots quantifying developmental potential across stromal sub-clusters. **(H and I)** Cross-study validation of cell identity. Dot plots show the correspondence between the identified **(H)** Stromal and **(I)** Endothelial sub-clusters and signatures from previously published datasets (e.g., Poon et al.), evaluated using AUCell enrichment scores. **See also Figure S5.**

Figure 6. Spatial phylogeography defines a recurrent "Spatial Resistance Triad" within hypoxic niches. (A) Systematic meta-analysis of spatial co-localization patterns. The heatmap displays the recurrence frequency of significant spatial associations between cNMF7 and other cell types across 48 integrated Visium samples (n=48). Columns represent varying percentile thresholds (10% to 50%) applied to MISTy importance scores to define significant co-localization. Rows (cell types) are hierarchically clustered into 5 distinct spatial modules based on their consistency of association. **(B)** Representative H&E staining of a GBM sample (UKF275) featuring Microvascular Proliferation (MVP). Insets (colored boxes) show high-magnification views of pathologist-annotated MVP regions. **(C)** Trajectory analysis quantifying the MVP niche using SPATA2. **Top:** Surface plot of the annotated MVP regions. **Middle:** Spatial gradient map visualization, where color intensity represents the computed distance from the nearest MVP structure. **Bottom:** Spatial projection of Hypoxia signature scores (AUCell) along the defined gradient. **(D and E)** Spatially resolved abundance profiles of the "Spatial Resistance Triad" members relative to MVP. **(D)** Heatmap and **(E)** corresponding trajectory line plots showing the abundance of cNMF7, E-MDSC.ADM.HIF1A, myCAF.02.COL6, and prolCAF.MKI67. Abundance is plotted as a function of distance from the MVP core, demonstrating a significant decreasing trend (enrichment in the niche). **(F–H)** Spatial feature plots visualizing the RCTD-deconvoluted proportions of the identified triad members on three independent Visium samples containing MVP regions: **(F)** UKF275, **(G)** UKF260, and **(H)** UKF259. **(I)** Representative H&E staining of a GBM sample (UKF313) exhibiting Pseudopalisading

Necrosis (PAN). Insets highlight the necrotic core and surrounding perinecrotic zone. **(J)** SPATA2 trajectory analysis for the PAN niche. Panels display the annotated necrotic regions (Top), distance gradient from the necrotic core (Middle), and hypoxia signature distribution (Bottom). **(K and L)** Distance-dependent abundance profiling relative to PAN. **(K)** Heatmap and **(L)** corresponding trajectory line plots showing the abundance of cNMF7, E-MDSC.ADM.HIF1A, myCAF.02.COL6, and myCAF.02.COL1. Abundance is plotted as a function of distance from the necrotic core, demonstrating a significant decreasing trend (enrichment in the niche). **(M–O)** Validation of spatial distributions. Feature plots display the RCTD-inferred proportions of the triad components in three independent samples with PAN structures: **(M)** UKF313, **(N)** UKF243, and **(O)** GBM03422. **See also Figure S6.**

Figure 7. The ECM-CD44 axis and reciprocal paracrine signaling sustain the Spatial Resistance Triad. (A) Dot plot visualizing the significant ECM-mediated communication probabilities from myCAFs (sender) to cNMF7 malignant cells and MDSCs (receivers), identified by CellChat analysis. **(B)** Bar plots quantifying the relative contribution of individual ligand-receptor pairs to the dominant **COLLAGEN** (left) and **FN1** (right) signaling pathways. **(C)** Expression dot plot of the key ligand-receptor pairs identified in **(A)** and **(B)**. Genes are grouped by interaction category (ECM-Receptor, Secreted Signaling, and Cell-Cell Contact) and plotted across the triad components (myCAFs, cNMF7, MDSCs). **(D and E)** Spatial validation of the ECM-CD44 axis within resistant niches. Spatial feature plots display the expression of ligands (*FN1, COL6A1, COL6A2, COL1A1, COL1A2, COL6A3*) and their cognate receptor (*CD44*) across three independent samples containing **(D)** Microvascular Proliferation (MVP) and **(E)** Pseudopalisading Necrosis (PAN) regions. **(F)** Dot plot summarizing the incoming **Secreted Signaling** interactions received by myCAFs from other TME components. **(G)** Expression profile of the ligand-receptor pairs mediating the signals received by myCAFs (from **F**), categorized into ECM-Receptor and Secreted Signaling, shown across the triad cell types. **(H)** Spatial feature plots of key paracrine mediators (*TNC, SPP1*) enriched in the MVP (left) and PAN (right) niches, confirming their co-localization with the resistance triad. **See also Figure S6.**

7.2 **Supplementary Figure Legend**

Figure S1. Quality control, batch correction, and cell type annotation of the GRIT-Atlas, related to Figure 1. (A) Representative sagittal contrast-enhanced MRI scans of five patients from the in-house Gusu cohort. **(B)** UMAP visualization of the aggregate dataset before (left) and after (right) batch effect correction using BBKNN. **(C)** UMAP embeddings colored by treatment group, sequencing modality (snRNA-seq vs. scRNA-seq), sequencing platform (e.g., 10x, SmartSeq2), and sample origin. **(D)** Feature plots displaying the expression of representative marker genes for the seven major cell types (arranged in 2 rows). **(E)** Heatmap of inferred Copy Number Variations (InferCNV) used to distinguish malignant cells, utilizing oligodendrocytes as the diploid reference. **(F)** UMAP projection distinguishing malignant cells (red, defined by CNV), astrocytes/neurons (blue), and oligodendrocytes (green). **(G)** Comparison of cell type proportions among the three treatment groups (pGBM, rGBM-R+C, and rGBM-ICB+Target) specifically within Mei et al.'s dataset.

Figure S2. Robustness of cNMF factorization and clinical validation of the cNMF7 signature, related to Figure 2. (A) Evaluation of cNMF model stability. Line plots display

the stability and reconstruction error across varying factorization ranks (K), guiding the selection of the optimal K value. **(B)** Consensus clustering heatmap for the selected K, demonstrating the robustness of cluster assignments across replicates. **(C and D)** Identification and exclusion of technical artifacts. Feature plots **(C)** and marker gene dot plots **(D)** characterize four excluded cNMF components associated with noise or confounding factors. **(E)** UMAP embeddings colored by sample origin, batch, treatment group, and sequencing modality (snRNA-seq vs. scRNA-seq) to confirm the absence of batch effects in the final integration. **(F)** Dot plot correlating the identified cNMF programs with previously established GBM cellular states (e.g., Neftel et al.) based on AUCell enrichment scores. **(G)** Transcriptional classification heatmap grouping cNMF programs into broader subtypes based on signature gene expression. **(H)** Dot plot comparing the expression of key functional genes involved in inflammation, invasion, hypoxia, anti-apoptosis, metabolic reprogramming, stemness, and stress between the cNMF7 state and other malignant populations. **(I)** Kaplan-Meier survival curves validating the prognostic significance of cNMF7. Patients from seven independent cohorts (CGGA, CPTAC, GLASS, GSE datasets, and TCGA) were stratified into high and low risk groups based on cNMF7 ssGSEA scores. Statistical significance was determined by the log-rank test.

Figure S3. Quality control and functional validation of myeloid sub-classifications, related to Figure 3. (A) Dot plot visualizing the expression of canonical lineage markers used to define the major myeloid classes (MG, BMDM, Mast, DC, Neutrophil, and Proliferating cells). **(B)** Box plot comparing the proportion of proliferating myeloid cells (normalized to CD45+ cells) across treatment groups. Statistical significance was assessed using the Wilcoxon rank-sum test. **(C)** UMAP embeddings colored by sample group, batch, and sequencing modality (snRNA-seq vs. scRNA-seq), confirming effective integration and absence of technical bias. **(D)** Gene Set Enrichment Analysis (GSEA) bubble plot highlighting the functional pathways enriched in the Mono.CD16.FCGR3A subset. **(E)** Radar plot mapping the functional orientation of all myeloid subsets onto four functional programs (microglial inflammatory program, scavenger immunosuppressive program, systemic inflammatory program and complement immunosuppressive program) defined by Miller et al.

Figure S4. Global characterization and quality assessment of the lymphoid compartment, related to Figure 4. (A) Global UMAP embedding of the lymphoid compartment, annotated by major lineages (CD4+ T cells, CD8+ T cells, NK cells, B cells, Plasma cells, and Tregs). **(B)** Dot plot showing the expression of canonical marker genes used to define the major lymphoid categories. **(C)** Box plots comparing the relative abundance of broad lymphoid lineages (B, CD4, CD8, NK) normalized to CD45+ cells across the four treatment groups. Statistical significance was determined by the Wilcoxon rank-sum test. **(D)** Assessment of batch effects and annotation resolution. The panel displays UMAP embeddings colored by Sample Group, Batch, Sequencing Modality (scRNA-seq vs. snRNA-seq), and medium-resolution cell annotations (including CD8+ CTL/Tex, CD8+ Tm/Tn, B cell subsets, CD4+ subsets, and NK subsets defined by *NKG2A/CD16/CD56* status). **(E)** Feature plots validating the molecular basis of NK cell sub-classification, highlighting the expression of *KLRC1* (NKG2A), *NCAM1* (CD56), and *FCGR3A* (CD16). **(F)** Box plots quantifying the proportions of medium-resolution lymphoid

subsets within the CD45+ compartment across treatment groups. Statistical significance was assessed using the Wilcoxon rank-sum test.

Figure S5. Annotation resolution and quality assessment of vascular and stromal cells, related to Figure 5. (A and B) Dot plots displaying the expression of lineage-defining markers for medium-resolution annotations of **(A)** Endothelial cells (Vein, Tip-like, Capillary, Arterial) and **(B)** Stromal cells (Smooth Muscle Cells [SMC], Pericytes [PC], Cancer-Associated Fibroblasts [CAF]). **(C)** Box plots comparing the proportional abundance of Stromal cells across the three treatment groups (pGBM, rGBM-R+C, and rGBM-ICB+Target), utilizing only non-sorted data to exclude technical bias. Statistical significance was determined by the Wilcoxon rank-sum test. **(D)** Comparison of cell type proportions specifically within Mei et al.'s dataset to validate trends observed in the integrated atlas. **(E and F)** Quality control UMAP embeddings for **(E)** Endothelial and **(F)** Stromal compartments. Plots are colored by medium-resolution annotation, sample group, batch, and sequencing modality (scRNA-seq vs. snRNA-seq), demonstrating robust integration.

Figure S6. Robustness of spatial co-localization inference and niche-specific enrichment, related to Figure 6 and Figure 7. (A) Comprehensive heatmap of MISTy importance scores across all 48 spatial transcriptomic samples. Rows represent individual samples, and columns represent cell types. Colors indicate the predictive importance of each cell type for the spatial distribution of the cNMF7 subpopulation. **(B and C)** Extended spatial trajectory analysis for identified spatial modules. **(B)** Heatmaps and **(C)** line plots display the distance-dependent abundance trends relative to MVP (left) and PAN (right) for **all** cell types within the spatially correlated modules identified in Figure 6A. These plots contextualize the specific enrichment of the "Spatial Resistance Triad" (shown in Figure 6D/K) against the broader background of spatially associated cells. **(D and E)** Extended CellChat analysis of outgoing signals from myCAFs. Dot plots display the significant **(D)** Secreted Signaling and **(E)** Cell-Cell Contact interactions originating from myCAFs to other cell types. **(F)** Spatial feature plots visualizing the expression of validated signaling molecules (*MIF, APP, CD74, CXCR4*) involved in the crosstalk identified in **(D)** and **(E)**. **(G and H)** Extended analysis of incoming signals to myCAFs. Dot plots show the significant **(G)** ECM-Receptor and **(H)** Cell-Cell Contact interactions received by myCAFs from the microenvironment. **(I)** Spatial feature plots of additional signaling mediators (*TNC, PTN, NCL, SDC2*) validating their enrichment in spatially restricted niches.

Figure S7. Clinical relevance, prognostic value, and pan-cancer validation of the resistance-associated ECM signature, related to Figure 7. (A) Dot plot validating the cell type specificity of the ECM signature genes (*COL1A1, COL1A2, COL6A1, COL6A2, COL6A3, FN1*). Expression is shown across the seven major cell lineages defined in the GRIT-Atlas. **(B)** Validation of ECM gene expression in the in-house Gusu cohort (n=49). Box plots compare bulk RNA-seq expression levels between normal brain tissue and gliomas of varying WHO grades. **(C)** Forest plots summarizing the meta-analysis of overall survival associations. Univariate Cox regression Hazard Ratios (HR) and 95% confidence intervals were calculated for each ECM gene across seven independent glioma cohorts (TCGA, CGGA325, CGGA693, GSE121720, GSE147352, GLASS, CPTAC) using a random-effects model. **(D)** Forest plots summarizing the meta-analysis of immunotherapy

response. Risk Ratios (RR) for objective response were evaluated for each ECM gene across multiple immunotherapy-treated cohorts covering diverse cancer types (GBM, Melanoma, RCC, BLCA, STAD). **(E)** Spatial validation using the Ivy Glioblastoma Atlas Project (Ivy GAP). Box plots display the expression of ECM signature genes across micro-dissected anatomical regions, confirming enrichment in peri-vascular and peri-necrotic zones (corresponding to MVP and PAN). **(F)** Correlation landscape between the ECM signature and the immunosuppressive microenvironment. The heatmap shows Spearman correlation coefficients between ECM genes and key immune signatures (T-cell exhaustion [*PDCD1, HAVCR2, TIGIT, LAG3*], MDSCs [*NOS2, ARG1*], M2-like TAMs [*CD163, TGFB1, CD274*], Tregs [*FOXP3, CTLA4, TNFRSF18*]) and functional pathways (Angiogenesis, EMT, Hypoxia) across seven cohorts. **(G)** Pan-cancer survival analysis. Heatmap displaying univariate Cox regression Hazard Ratios for the six ECM genes across 33 cancer types from the TCGA database. **(H)** Pan-cancer proteomic validation. Dot plot visualizing the differential protein expression of the ECM signature genes across 10 cancer types from the CPTAC dataset.

7.3 **Supplementary Table Legend**

Table S1. Summary of datasets and patient clinicopathological metadata, related to Methods and Figure 1. This table provides a detailed catalog of the 17 single-cell/single-nucleus RNA sequencing (sc/snRNA-seq) datasets, 48 spatial transcriptomics (ST) sections, and bulk RNA-seq cohorts integrated into the GRIT-Atlas.

Table S2. Comprehensive list of differentially expressed genes (DEGs) for all cell subpopulations, related to Figures 1-5. Complete output of Seurat's *FindAllMarkers* analysis for each major lineage (Malignant, Myeloid, Lymphoid, Stromal, and Endothelial). The table includes gene symbols, p-values, adjusted p-values, average log2-fold changes (log2FC), and the percentage of cells expressing the gene in the cluster versus all other clusters.

Table S3. Curated representative marker genes for major cell lineages and subpopulations, related to Figures 2-5. A filtered selection of highly specific marker genes (3-5 per subpopulation) used for subcluster characterization across malignant states, myeloid subsets, lymphoid populations, and stromal/endothelial variants.

Table S4. Summary of Published Gene Signatures for Cell Type Benchmarking and Validation, Related to Methods and Figures 2–5. Cell type identification and validation were performed through systematic benchmarking against established gene signatures from high-resolution glioblastoma (GBM) and pan-cancer studies. For each cell subpopulation within the GRIT-Atlas, differentially expressed genes (DEGs) were identified using the FindMarkers function in Seurat, with the top 100 most significant genes selected as cluster-specific signatures. These signatures were quantitatively compared with published marker sets using Seurat's AddModuleScore function to compute enrichment scores for specific cellular states. For malignant cells, classifications were benchmarked against four major frameworks: the AC/NPC/OPC/MES-like states (Ruiz-Moreno et al. and Neftel et al.) , the T1–T10 malignant cell system (Jackson et al.) , and 41 consensus meta-programs representing transcriptional intratumoral heterogeneity (Gavish et al.). Myeloid populations were evaluated against functionally characterized subsets, including early progenitor MDSCs (Jackson et al.), hypoxia-responsive TAMs (Wang et al.), GPNMB+

MDMs (Du et al.), and four consensus immunomodulatory programs (microglial inflammatory, systemic inflammatory, complement immunosuppressive, and scavenger immunosuppressive; Miller et al.). Endothelial cell signatures were integrated from high-resolution blood-brain and blood-tumor barrier atlases distinguishing permeability (GBM-EC type 1/2) and anatomical phenotypes (Peripheral Pe1 vs. Tumor Core Co1). Stromal components were validated against three complementary schemes: the mesenchymal stromal cell system (Poon et al.), the myofibroblastic/inflammatory/antigen-presenting CAF taxonomy (Gao et al.), and the niche-specific COL6A3+ tumor-associated fibroblast (TAF) module (Du et al.).

Table S5. Spatial inter-cellular association scores calculated via MISTy across 48 patient sections, related to Figure 6. Summary of importance values quantifying the spatial relationships (co-localization or exclusion) between the cNMF7 malignant subpopulation and all other cell subtypes. Data are presented for each individual sample, facilitating the identification of recurrent spatial relationship patterns within the tumor microenvironment.

8 Data and Code Availability

8.1 Data availability

The Glioblastoma Resistance Insights from Treatment Atlas (GRIT-Atlas) represents a comprehensive single-cell and spatially resolved transcriptomic resource for IDH-wildtype glioblastoma. All processed data objects generated in this study have been deposited at Zenodo and are publicly available as of the date of publication at https://doi.org/10.5281/zenodo.18009414. This repository includes the master Seurat/AnnData object encompassing 978,065 high-quality cells, high-resolution sub-lineage objects for the malignant, myeloid, lymphoid, stromal, and endothelial compartments , as well as the RCTD deconvolution results and MistyR spatial importance matrices for 48 Visium sections. Primary raw sequencing data utilized for this atlas were sourced from public repositories, including GEO, EGA, and SRA; specific accession numbers and metadata for the 296 samples integrated into this study are provided in Table S1.

8.2 Code availability

All original code and computational pipelines developed for the construction and analysis of the GRIT-Atlas have been deposited at GitHub and are publicly available as of the date of publication: https://github.com/Dr-fly/GRIT-Atlas. The repository contains detailed, reproducible workflows for single-cell preprocessing, BBKNN-based batch integration, malignant functional state characterization via consensus NMF, spatial deconvolution using RCTD , and intercellular communication modeling via CellChat. These scripts are implemented in Python (v3.10.12) and R (v4.3.2) environments. A stable version of the code specifically used to generate the final results reported in this paper is also archived at Zenodo alongside the processed data objects.

9 Acknowledgements

Not applicable.

10 Author contributions

F.W., Z.C., and Z.W. conceived and designed the study . F.W. led the development of methodologies and computational software with support from R.H. and H.L. . Formal data analysis and visualization were performed by F.W., R.H., H.L., Y.B., C.Y., and G.Z.. F.W. coordinated the investigation and resource collection with significant contributions from X.W., W.C., Y.L., Y.N.Z., D.L., Y.Q., J.Z., B.G., C.M., H.D., Y.B.Y., Y.L.Z., and T.S. . Data curation was managed by F.W., R.H., H.L., and Y.B. . F.W. wrote the original draft of the manuscript , and F.W., Z.C., and Z.W. performed critical revisions and intellectual editing. Overall project supervision and funding acquisition were provided by Z.C. and Z.W.

11 Funding

This work was supported by the Innovative Technology Class A grant of the First Affiliated Hospital of Soochow University [grant number 0499980301001], National Natural Science Foundation of China [grant number 82571477] and National Natural Science Foundation

of China [grant number 82201445].

12 Reference

1. Miller, K.D., Ostrom, Q.T., Kruchko, C., Patil, N., Tihan, T., Cioffi, G., Fuchs, H.E., Waite, K.A., Jemal, A., Siegel, R.L., and Barnholtz-Sloan, J.S. (2021). Brain and other central nervous system tumor statistics, 2021. CA Cancer J Clin *71*, 381-406. 10.3322/caac.21693.
2. Wen, P.Y., Weller, M., Lee, E.Q., Alexander, B.M., Barnholtz-Sloan, J.S., Barthel, F.P., Batchelor, T.T., Bindra, R.S., Chang, S.M., Chiocca, E.A., et al. (2020). Glioblastoma in adults: a Society for Neuro-Oncology (SNO) and European Society of Neuro-Oncology (EANO) consensus review on current management and future directions. Neuro Oncol *22*, 1073-1113. 10.1093/neuonc/noaa106.
3. Schaff, L.R., and Mellinghoff, I.K. (2023). Glioblastoma and Other Primary Brain Malignancies in Adults: A Review. Jama *329*, 574-587. 10.1001/jama.2023.0023.
4. Yabo, Y.A., Niclou, S.P., and Golebiewska, A. (2022). Cancer cell heterogeneity and plasticity: A paradigm shift in glioblastoma. Neuro Oncol *24*, 669-682. 10.1093/neuonc/noab269.
5. Lin, H., Liu, C., Hu, A., Zhang, D., Yang, H., and Mao, Y. (2024). Understanding the immunosuppressive microenvironment of glioma: mechanistic insights and clinical perspectives. J Hematol Oncol *17*, 31. 10.1186/s13045-024-01544-7.
6. Hendriksen, J.D., Locallo, A., Maarup, S., Debnath, O., Ishaque, N., Hasselbach, B., Skjøth-Rasmussen, J., Yde, C.W., Poulsen, H.S., Lassen, U., and Weischenfeldt, J. (2024). Immunotherapy drives mesenchymal tumor cell state shift and TME immune response in glioblastoma patients. Neuro Oncol *26*, 1453-1466. 10.1093/neuonc/noae085.
7. Gupta, P., Dang, M., Oberai, S., Migliozzi, S., Trivedi, R., Kumar, G., Peshoff, M., Milam, N., Ahmed, A., Bojja, K., et al. (2024). Immune landscape of isocitrate dehydrogenase-stratified primary and recurrent human gliomas. Neuro Oncol *26*, 2239-2255. 10.1093/neuonc/noae139.
8. Bunse, L., Bunse, T., Kilian, M., Quintana, F.J., and Platten, M. (2025). The immunology of brain tumors. Sci Immunol *10*, eads0449. 10.1126/sciimmunol.ads0449.
9. Mahdi, J., Trivedi, V., and Monje, M. (2025). The promise of immunotherapy for central nervous system tumours. Nat Rev Immunol. 10.1038/s41577-025-01227-5.
10. Spitzer, A., Johnson, K.C., Nomura, M., Garofano, L., Nehar-Belaid, D., Darnell, N.G., Greenwald, A.C., Bussema, L., Oh, Y.T., Varn, F.S., et al. (2025). Deciphering the longitudinal trajectories of glioblastoma ecosystems by integrative single-cell genomics. Nat Genet *57*, 1168-1178. 10.1038/s41588-025-02168-4.
11. Nomura, M., Spitzer, A., Johnson, K.C., Garofano, L., Nehar-Belaid, D., Galili Darnell, N., Greenwald, A.C., Bussema, L., Oh, Y.T., Varn, F.S., et al. (2025). The multilayered transcriptional architecture of glioblastoma ecosystems. Nat Genet *57*, 1155-1167. 10.1038/s41588-025-02167-5.
12. Lee, A.H., Sun, L., Mochizuki, A.Y., Reynoso, J.G., Orpilla, J., Chow, F., Kienzler, J.C., Everson, R.G., Nathanson, D.A., Bensinger, S.J., et al. (2021). Neoadjuvant PD-1 blockade induces T cell and cDC1 activation but fails to overcome the immunosuppressive tumor associated macrophages in recurrent glioblastoma. Nat

Commun *12*, 6938. 10.1038/s41467-021-26940-2.

13. Mei, Y., Wang, X., Zhang, J., Liu, D., He, J., Huang, C., Liao, J., Wang, Y., Feng, Y., Li, H., et al. (2023). Siglec-9 acts as an immune-checkpoint molecule on macrophages in glioblastoma, restricting T-cell priming and immunotherapy response. Nat Cancer *4*, 1273-1291. 10.1038/s43018-023-00598-9.
14. Pombo Antunes, A.R., Scheyltjens, I., Lodi, F., Messiaen, J., Antoranz, A., Duerinck, J., Kancheva, D., Martens, L., De Vlaminck, K., Van Hove, H., et al. (2021). Single-cell profiling of myeloid cells in glioblastoma across species and disease stage reveals macrophage competition and specialization. Nat Neurosci *24*, 595-610. 10.1038/s41593-020-00789-y.
15. Poon, C.C., Herbrich, S.M., Chen, Y., Hossain, A., Fuller, G.N., Jindal, S., Basu, S., Ledbetter, D., Macaluso, M., Phillips, L.M., et al. (2025). Mesenchymal Stem Cells and Fibroblasts Contribute to Microvascular Proliferation in Glioblastoma and are Correlated with Immunosuppression and Poor Outcome. Cancer Immunol Res *13*, 804-820. 10.1158/2326-6066.Cir-24-0743.
16. Migliozzi, S., Adabbo, B., Garofano, L., Wu, F., Davila, P., Komotar, R.J., Ivan, M.E., Shah, A.H., Currall, B.B., Williams, S., et al. (2025). Restraint of cancer cell plasticity by spatial homotypic clustering. Cancer Cell *43*, 2206-2223.e2210. 10.1016/j.ccell.2025.08.009.
17. Artzi, S.B., Klausen, M.N., Harwood, D.S.L., Michaelsen, S.R., Maarup, S.B., Locallo, A., Fougner, V., Bager, N.S., Hammouda, N.M., Nørøxe, D.S., et al. (2025). Spatial transcriptomic analysis reveals lack of response to PD-1 blockade in recurrent glioblastoma. Acta Neuropathol *150*, 29. 10.1007/s00401-025-02937-9.
18. Puchalski, R.B., Shah, N., Miller, J., Dalley, R., Nomura, S.R., Yoon, J.G., Smith, K.A., Lankerovich, M., Bertagnolli, D., Bickley, K., et al. (2018). An anatomic transcriptional atlas of human glioblastoma. Science *360*, 660-663. 10.1126/science.aaf2666.
19. Huse, J.T., and Holland, E.C. (2010). Targeting brain cancer: advances in the molecular pathology of malignant glioma and medulloblastoma. Nat Rev Cancer *10*, 319-331. 10.1038/nrc2818.
20. Stupp, R., Mason, W.P., van den Bent, M.J., Weller, M., Fisher, B., Taphoorn, M.J., Belanger, K., Brandes, A.A., Marosi, C., Bogdahn, U., et al. (2005). Radiotherapy plus concomitant and adjuvant temozolomide for glioblastoma. N Engl J Med *352*, 987-996. 10.1056/NEJMoa043330.
21. Nassiri, F., Patil, V., Yefet, L.S., Singh, O., Liu, J., Dang, R.M.A., Yamaguchi, T.N., Daras, M., Cloughesy, T.F., Colman, H., et al. (2023). Oncolytic DNX-2401 virotherapy plus pembrolizumab in recurrent glioblastoma: a phase 1/2 trial. Nat Med *29*, 1370-1378. 10.1038/s41591-023-02347-y.
22. Wolock, S.L., Lopez, R., and Klein, A.M. (2019). Scrublet: Computational Identification of Cell Doublets in Single-Cell Transcriptomic Data. Cell Syst *8*, 281-291.e289. 10.1016/j.cels.2018.11.005.
23. Mathewson, N.D., Ashenberg, O., Tirosh, I., Gritsch, S., Perez, E.M., Marx, S., Jerby-Arnon, L., Chanoch-Myers, R., Hara, T., Richman, A.R., et al. (2021). Inhibitory CD161 receptor identified in glioma-infiltrating T cells by single-cell analysis. Cell *184*, 1281-1298.e1226. 10.1016/j.cell.2021.01.022.

24. Neftel, C., Laffy, J., Filbin, M.G., Hara, T., Shore, M.E., Rahme, G.J., Richman, A.R., Silverbush, D., Shaw, M.L., Hebert, C.M., et al. (2019). An Integrative Model of Cellular States, Plasticity, and Genetics for Glioblastoma. Cell *178*, 835-849.e821. 10.1016/j.cell.2019.06.024.
25. Sun, H.F., Li, L.D., Lao, I.W., Li, X., Xu, B.J., Cao, Y.Q., and Jin, W. (2022). Single-cell RNA sequencing reveals cellular and molecular reprograming landscape of gliomas and lung cancer brain metastases. Clin Transl Med *12*, e1101. 10.1002/ctm2.1101.
26. Schmassmann, P., Roux, J., Dettling, S., Hogan, S., Shekarian, T., Martins, T.A., Ritz, M.F., Herter, S., Bacac, M., and Hutter, G. (2023). Single-cell characterization of human GBM reveals regional differences in tumor-infiltrating leukocyte activation. Elife *12*. 10.7554/eLife.92678.
27. Müller, S., Di Lullo, E., Bhaduri, A., Alvarado, B., Yagnik, G., Kohanbash, G., Aghi, M., and Diaz, A. (2018). A single-cell atlas of human glioblastoma reveals a single axis of phenotype in tumor-propagating cells. bioRxiv, 377606. 10.1101/377606.
28. Wolf, F.A., Angerer, P., and Theis, F.J. (2018). SCANPY: large-scale single-cell gene expression data analysis. Genome Biol *19*, 15. 10.1186/s13059-017-1382-0.
29. Polański, K., Young, M.D., Miao, Z., Meyer, K.B., Teichmann, S.A., and Park, J.E. (2020). BBKNN: fast batch alignment of single cell transcriptomes. Bioinformatics *36*, 964-965. 10.1093/bioinformatics/btz625.
30. Zhou, Y., Zhou, B., Pache, L., Chang, M., Khodabakhshi, A.H., Tanaseichuk, O., Benner, C., and Chanda, S.K. (2019). Metascape provides a biologist-oriented resource for the analysis of systems-level datasets. Nat Commun *10*, 1523. 10.1038/s41467-019-09234-6.
31. Patel, A.P., Tirosh, I., Trombetta, J.J., Shalek, A.K., Gillespie, S.M., Wakimoto, H., Cahill, D.P., Nahed, B.V., Curry, W.T., Martuza, R.L., et al. (2014). Single-cell RNA-seq highlights intratumoral heterogeneity in primary glioblastoma. Science *344*, 1396-1401. 10.1126/science.1254257.
32. Brennan, C.W., Verhaak, R.G., McKenna, A., Campos, B., Noushmehr, H., Salama, S.R., Zheng, S., Chakravarty, D., Sanborn, J.Z., Berman, S.H., et al. (2013). The somatic genomic landscape of glioblastoma. Cell *155*, 462-477. 10.1016/j.cell.2013.09.034.
33. Zeng, Z., Ma, Y., Hu, L., Tan, B., Liu, P., Wang, Y., Xing, C., Xiong, Y., and Du, H. (2024). OmicVerse: a framework for bridging and deepening insights across bulk and single-cell sequencing. Nat Commun *15*, 5983. 10.1038/s41467-024-50194-3.
34. Hao, Y., Hao, S., Andersen-Nissen, E., Mauck, W.M., 3rd, Zheng, S., Butler, A., Lee, M.J., Wilk, A.J., Darby, C., Zager, M., et al. (2021). Integrated analysis of multimodal single-cell data. Cell *184*, 3573-3587.e3529. 10.1016/j.cell.2021.04.048.
35. Zhang, L., Yu, X., Zheng, L., Zhang, Y., Li, Y., Fang, Q., Gao, R., Kang, B., Zhang, Q., Huang, J.Y., et al. (2018). Lineage tracking reveals dynamic relationships of T cells in colorectal cancer. Nature *564*, 268-272. 10.1038/s41586-018-0694-x.
36. Ruiz-Moreno, C., Salas, S.M., Samuelsson, E., Minaeva, M., Ibarra, I., Grillo, M., Brandner, S., Roy, A., Forsberg-Nilsson, K., Kranendonk, M.E.G., et al. (2025). Charting the single-cell and spatial landscape of IDH-wild-type glioblastoma with GBmap. Neuro Oncol *27*, 2281-2295. 10.1093/neuonc/noaf113.

37. Jackson, C., Cherry, C., Bom, S., Dykema, A.G., Wang, R., Thompson, E., Zhang, M., Li, R., Ji, Z., Hou, W., et al. (2025). Distinct myeloid-derived suppressor cell populations in human glioblastoma. Science *387*, eabm5214. 10.1126/science.abm5214.
38. Gavish, A., Tyler, M., Greenwald, A.C., Hoefflin, R., Simkin, D., Tschernichovsky, R., Galili Darnell, N., Somech, E., Barbolin, C., Antman, T., et al. (2023). Hallmarks of transcriptional intratumour heterogeneity across a thousand tumours. Nature *618*, 598-606. 10.1038/s41586-023-06130-4.
39. Wang, W., Li, T., Cheng, Y., Li, F., Qi, S., Mao, M., Wu, J., Liu, Q., Zhang, X., Li, X., et al. (2024). Identification of hypoxic macrophages in glioblastoma with therapeutic potential for vasculature normalization. Cancer Cell *42*, 815-832.e812. 10.1016/j.ccell.2024.03.013.
40. Du, Y., Long, X., Li, X., Guan, F., Gao, W., Deng, K., Wang, S., Lin, X., Huang, M., She, X., et al. (2025). Spatial-reprogramming derived GPNMB(+) macrophages interact with COL6A3(+) fibroblasts to enhance vascular fibrosis in glioblastoma. Genome Med *17*, 136. 10.1186/s13073-025-01553-2.
41. Miller, T.E., El Farran, C.A., Couturier, C.P., Chen, Z., D'Antonio, J.P., Verga, J., Villanueva, M.A., Gonzalez Castro, L.N., Tong, Y.E., Saadi, T.A., et al. (2025). Programs, origins and immunomodulatory functions of myeloid cells in glioma. Nature *640*, 1072-1082. 10.1038/s41586-025-08633-8.
42. Xie, Y., Yang, F., He, L., Huang, H., Chao, M., Cao, H., Hu, Y., Fan, Z., Zhai, Y., Zhao, W., et al. (2024). Single-cell dissection of the human blood-brain barrier and glioma blood-tumor barrier. Neuron *112*, 3089-3105.e3087. 10.1016/j.neuron.2024.07.026.
43. Xie, Y., He, L., Lugano, R., Zhang, Y., Cao, H., He, Q., Chao, M., Liu, B., Cao, Q., Wang, J., et al. (2021). Key molecular alterations in endothelial cells in human glioblastoma uncovered through single-cell RNA sequencing. JCI Insight *6*. 10.1172/jci.insight.150861.
44. Gao, Y., Li, J., Cheng, W., Diao, T., Liu, H., Bo, Y., Liu, C., Zhou, W., Chen, M., Zhang, Y., et al. (2024). Cross-tissue human fibroblast atlas reveals myofibroblast subtypes with distinct roles in immune modulation. Cancer Cell *42*, 1764-1783.e1710. 10.1016/j.ccell.2024.08.020.
45. Badia, I.M.P., Vélez Santiago, J., Braunger, J., Geiss, C., Dimitrov, D., Müller-Dott, S., Taus, P., Dugourd, A., Holland, C.H., Ramirez Flores, R.O., and Saez-Rodriguez, J. (2022). decoupleR: ensemble of computational methods to infer biological activities from omics data. Bioinform Adv *2*, vbac016. 10.1093/bioadv/vbac016.
46. Xu, S., Hu, E., Cai, Y., Xie, Z., Luo, X., Zhan, L., Tang, W., Wang, Q., Liu, B., Wang, R., et al. (2024). Using clusterProfiler to characterize multiomics data. Nat Protoc *19*, 3292-3320. 10.1038/s41596-024-01020-z.
47. Kang, M., Gulati, G.S., Brown, E.L., Qi, Z., Avagyan, S., Armenteros, J.J.A., Gleyzer, R., Zhang, W., Steen, C.B., D'Silva, J.P., et al. (2025). Improved reconstruction of single-cell developmental potential with CytoTRACE 2. Nat Methods *22*, 2258-2263. 10.1038/s41592-025-02857-2.
48. Van de Sande, B., Flerin, C., Davie, K., De Waegeneer, M., Hulselmans, G., Aibar, S., Seurinck, R., Saelens, W., Cannoodt, R., Rouchon, Q., et al. (2020). A scalable SCENIC workflow for single-cell gene regulatory network analysis. Nat Protoc *15*,

2247-2276. 10.1038/s41596-020-0336-2.
49. Ravi, V.M., Will, P., Kueckelhaus, J., Sun, N., Joseph, K., Salié, H., Vollmer, L., Kuliesiute, U., von Ehr, J., Benotmane, J.K., et al. (2022). Spatially resolved multi-omics deciphers bidirectional tumor-host interdependence in glioblastoma. Cancer Cell *40*, 639-655.e613. 10.1016/j.ccell.2022.05.009.
50. Ren, Y., Huang, Z., Zhou, L., Xiao, P., Song, J., He, P., Xie, C., Zhou, R., Li, M., Dong, X., et al. (2023). Spatial transcriptomics reveals niche-specific enrichment and vulnerabilities of radial glial stem-like cells in malignant gliomas. Nat Commun *14*, 1028. 10.1038/s41467-023-36707-6.
51. Greenwald, A.C., Darnell, N.G., Hoefflin, R., Simkin, D., Mount, C.W., Gonzalez Castro, L.N., Harnik, Y., Dumont, S., Hirsch, D., Nomura, M., et al. (2024). Integrative spatial analysis reveals a multi-layered organization of glioblastoma. Cell *187*, 2485-2501.e2426. 10.1016/j.cell.2024.03.029.
52. Cable, D.M., Murray, E., Zou, L.S., Goeva, A., Macosko, E.Z., Chen, F., and Irizarry, R.A. (2022). Robust decomposition of cell type mixtures in spatial transcriptomics. Nat Biotechnol *40*, 517-526. 10.1038/s41587-021-00830-w.
53. Tanevski, J., Flores, R.O.R., Gabor, A., Schapiro, D., and Saez-Rodriguez, J. (2022). Explainable multiview framework for dissecting spatial relationships from highly multiplexed data. Genome Biol *23*, 97. 10.1186/s13059-022-02663-5.
54. Kueckelhaus, J., Frerich, S., Kada-Benotmane, J., Koupourtidou, C., Ninkovic, J., Dichgans, M., Beck, J., Schnell, O., and Heiland, D.H. (2024). Inferring histology-associated gene expression gradients in spatial transcriptomic studies. Nat Commun *15*, 7280. 10.1038/s41467-024-50904-x.
55. Jin, S., Guerrero-Juarez, C.F., Zhang, L., Chang, I., Ramos, R., Kuan, C.H., Myung, P., Plikus, M.V., and Nie, Q. (2021). Inference and analysis of cell-cell communication using CellChat. Nat Commun *12*, 1088. 10.1038/s41467-021-21246-9.
56. Balduzzi, S., Rücker, G., and Schwarzer, G. (2019). How to perform a meta-analysis with R: a practical tutorial. Evid Based Ment Health *22*, 153-160. 10.1136/ebmental-2019-300117.
57. Garofano, L., Migliozzi, S., Oh, Y.T., D'Angelo, F., Najac, R.D., Ko, A., Frangaj, B., Caruso, F.P., Yu, K., Yuan, J., et al. (2021). Pathway-based classification of glioblastoma uncovers a mitochondrial subtype with therapeutic vulnerabilities. Nat Cancer *2*, 141-156. 10.1038/s43018-020-00159-4.
58. Kim, K.H., Migliozzi, S., Koo, H., Hong, J.H., Park, S.M., Kim, S., Kwon, H.J., Ha, S., Garofano, L., Oh, Y.T., et al. (2024). Integrated proteogenomic characterization of glioblastoma evolution. Cancer Cell *42*, 358-377.e358. 10.1016/j.ccell.2023.12.015.
59. Varn, F.S., Johnson, K.C., Martinek, J., Huse, J.T., Nasrallah, M.P., Wesseling, P., Cooper, L.A.D., Malta, T.M., Wade, T.E., Sabedot, T.S., et al. (2022). Glioma progression is shaped by genetic evolution and microenvironment interactions. Cell *185*, 2184-2199.e2116. 10.1016/j.cell.2022.04.038.
60. Guo, Y., Hong, W., Zhang, P., Han, D., Fang, Y., Tu, J., and Wei, W. (2020). Abnormal polarization of macrophage-like cells in the peripheral blood of patients with glioma. Oncol Lett *20*, 947-954. 10.3892/ol.2020.11602.
61. Lehman, N., Kowalska, W., Zarobkiewicz, M., Mazurek, M., Mrozowska, K., Bojarska-

Junak, A., and Rola, R. (2023). Pro- vs. Anti-Inflammatory Features of Monocyte Subsets in Glioma Patients. Int J Mol Sci *24*. 10.3390/ijms24031879.

62. Ma, T., Chu, X., Wang, J., Li, X., Zhang, Y., Tong, D., Xu, W., Dang, G., Qi, L., Miao, Y., et al. (2025). Pan-Cancer Analyses Refine the Single-Cell Portrait of Tumor-Infiltrating Dendritic Cells. Cancer Res *85*, 3596-3613. 10.1158/0008-5472.Can-24-3595.
63. Carrette, F., and Vivier, E. (2023). NKG2A blocks the anti-metastatic functions of natural killer cells. Cancer Cell *41*, 232-234. 10.1016/j.ccell.2023.01.008.
64. Wang, A.Z., Mashimo, B.L., Schaettler, M.O., Sherpa, N.D., Leavitt, L.A., Livingstone, A.J., Khan, S.M., Li, M., Anzaldua-Campos, M.I., Bradley, J.D., et al. (2024). Glioblastoma-Infiltrating CD8+ T Cells Are Predominantly a Clonally Expanded GZMK+ Effector Population. Cancer Discov *14*, 1106-1131. 10.1158/2159-8290.Cd-23-0913.
65. Sun, Q., and Dong, C. (2025). Regulators of CD8(+) T cell exhaustion. Nat Rev Immunol. 10.1038/s41577-025-01221-x.
66. Cakmak, P., Lun, J.H., Singh, A., Macas, J., Schupp, J., Schuck, J., Mahmoud, Z., Köhler, M., Starzetz, T., Burger, M.C., et al. (2025). Spatial immune profiling defines a subset of human gliomas with functional tertiary lymphoid structures. Immunity *58*, 2847-2863.e2848. 10.1016/j.immuni.2025.09.018.
67. Liu, B., Hu, X., Feng, K., Gao, R., Xue, Z., Zhang, S., Zhang, Y., Corse, E., Hu, Y., Han, W., and Zhang, Z. (2022). Temporal single-cell tracing reveals clonal revival and expansion of precursor exhausted T cells during anti-PD-1 therapy in lung cancer. Nat Cancer *3*, 108-121. 10.1038/s43018-021-00292-8.
68. Jain, S., Rick, J.W., Joshi, R.S., Beniwal, A., Spatz, J., Gill, S., Chang, A.C., Choudhary, N., Nguyen, A.T., Sudhir, S., et al. (2023). Single-cell RNA sequencing and spatial transcriptomics reveal cancer-associated fibroblasts in glioblastoma with protumoral effects. J Clin Invest *133*. 10.1172/jci147087.
69. Caligiuri, G., and Tuveson, D.A. (2023). Activated fibroblasts in cancer: Perspectives and challenges. Cancer Cell *41*, 434-449. 10.1016/j.ccell.2023.02.015.
70. Boeker, V., and Kalluri, R. (2025). Insights into the relevance of targeting fibroblasts to control cancer. Cell Rep Med *6*, 102395. 10.1016/j.xcrm.2025.102395.
71. Jia, H., Chen, X., Zhang, L., and Chen, M. (2025). Cancer associated fibroblasts in cancer development and therapy. J Hematol Oncol *18*, 36. 10.1186/s13045-025-01688-0.
72. Calabrese, C., Poppleton, H., Kocak, M., Hogg, T.L., Fuller, C., Hamner, B., Oh, E.Y., Gaber, M.W., Finklestein, D., Allen, M., et al. (2007). A perivascular niche for brain tumor stem cells. Cancer Cell *11*, 69-82. 10.1016/j.ccr.2006.11.020.
73. Chen, C., Zhao, S., Karnad, A., and Freeman, J.W. (2018). The biology and role of CD44 in cancer progression: therapeutic implications. J Hematol Oncol *11*, 64. 10.1186/s13045-018-0605-5.
74. Johansson, E., Grassi, E.S., Pantazopoulou, V., Tong, B., Lindgren, D., Berg, T.J., Pietras, E.J., Axelson, H., and Pietras, A. (2017). CD44 Interacts with HIF-2α to Modulate the Hypoxic Phenotype of Perinecrotic and Perivascular Glioma Cells. Cell Rep *20*, 1641-1653. 10.1016/j.celrep.2017.07.049.
75. Pietras, A., Katz, A.M., Ekström, E.J., Wee, B., Halliday, J.J., Pitter, K.L., Werbeck, J.L., Amankulor, N.M., Huse, J.T., and Holland, E.C. (2014). Osteopontin-CD44 signaling in

the glioma perivascular niche enhances cancer stem cell phenotypes and promotes aggressive tumor growth. Cell Stem Cell *14*, 357-369. 10.1016/j.stem.2014.01.005.

76. Zuo, Y., Jin, Y., Li, G., Ming, Y., Fan, T., Pan, Y., Yao, X., and Peng, Y. (2025). Spatial transcriptomic analysis of tumor microenvironment in esophageal squamous cell carcinoma with HIV infection. Mol Cancer *24*, 54. 10.1186/s12943-025-02248-3.
77. Li, T., Li, X., Xiang, X., Huang, J., Shen, X., Wang, M., Jiang, J., Shao, S., Li, Z., Xie, T., et al. (2025). Regenerative Hair Pigmentation via Skin Organoids: Adaptive Patterning Mediated by Collagen VI and Semaphorin 3C. Adv Sci (Weinh) *12*, e02436. 10.1002/advs.202502436.
78. Merzak, A., Koocheckpour, S., and Pilkington, G.J. (1994). CD44 mediates human glioma cell adhesion and invasion in vitro. Cancer Res *54*, 3988-3992.
79. Turtoi, A., Blomme, A., Bianchi, E., Maris, P., Vannozzi, R., Naccarato, A.G., Delvenne, P., De Pauw, E., Bevilacqua, G., and Castronovo, V. (2014). Accessibilome of human glioblastoma: collagen-VI-alpha-1 is a new target and a marker of poor outcome. J Proteome Res *13*, 5660-5669. 10.1021/pr500657w.
80. Cescon, M., Rampazzo, E., Bresolin, S., Da Ros, F., Manfreda, L., Cani, A., Della Puppa, A., Braghetta, P., Bonaldo, P., and Persano, L. (2023). Collagen VI sustains cell stemness and chemotherapy resistance in glioblastoma. Cell Mol Life Sci *80*, 233. 10.1007/s00018-023-04887-5.
81. Galbo, P.M., Jr., Madsen, A.T., Liu, Y., Peng, M., Wei, Y., Ciesielski, M.J., Fenstermaker, R.A., Graff, S., Montagna, C., Segall, J.E., et al. (2024). Functional Contribution and Clinical Implication of Cancer-Associated Fibroblasts in Glioblastoma. Clin Cancer Res *30*, 865-876. 10.1158/1078-0432.Ccr-23-0493.
82. Chen, J., Liu, Y., Lan, J., Liu, H., Tang, Q., Li, Z., Qiu, X., Hu, W., Xie, J., Feng, Y., et al. (2024). Identification and validation of COL6A1 as a novel target for tumor electric field therapy in glioblastoma. CNS Neurosci Ther *30*, e14802. 10.1111/cns.14802.
83. Kim, S.M., Lim, E.J., Yoo, K.C., Zhao, Y., Kang, J.H., Lim, E.J., Shin, I., Kang, S.G., Lim, H.W., and Lee, S.J. (2022). Glioblastoma-educated mesenchymal stem-like cells promote glioblastoma infiltration via extracellular matrix remodelling in the tumour microenvironment. Clin Transl Med *12*, e997. 10.1002/ctm2.997.
84. Ji, L., Xia, D., Zhou, Y., Hu, Y., Yang, Z., Yin, Y., Wang, J., Zhang, B., Gong, L., Li, K., et al. (2025). Spatial transcriptomics and multi-omics reveal relapse and resistance mechanisms of EndMT-derived CAFs mediated by TNC and FLNC in glioblastoma. J Transl Med *23*, 702. 10.1186/s12967-025-06743-5.
85. Wei, Y., Geng, S., Si, Y., Yang, Y., Chen, Q., Huang, S., Chen, X., Xu, W., Liu, Y., and Jiang, J. (2024). The Interaction between Collagen 1 and High Mannose Type CD133 Up-Regulates Glutamine Transporter SLC1A5 to Promote the Tumorigenesis of Glioblastoma Stem Cells. Adv Sci (Weinh) *11*, e2306715. 10.1002/advs.202306715.

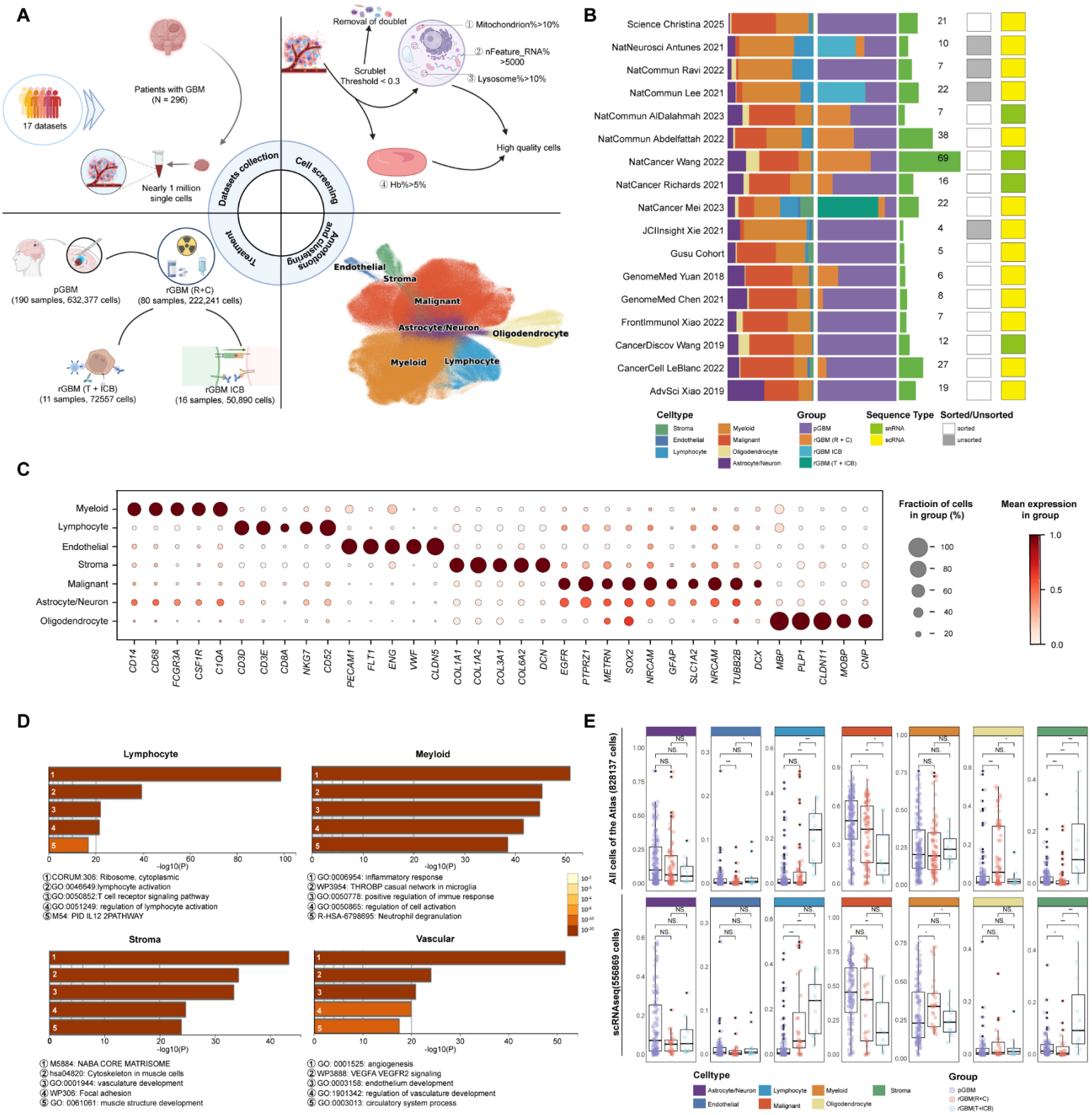

Figure 1 Construction and single-cell landscape of the GRIT-Atlas in IDH-wildtype glioblastoma.

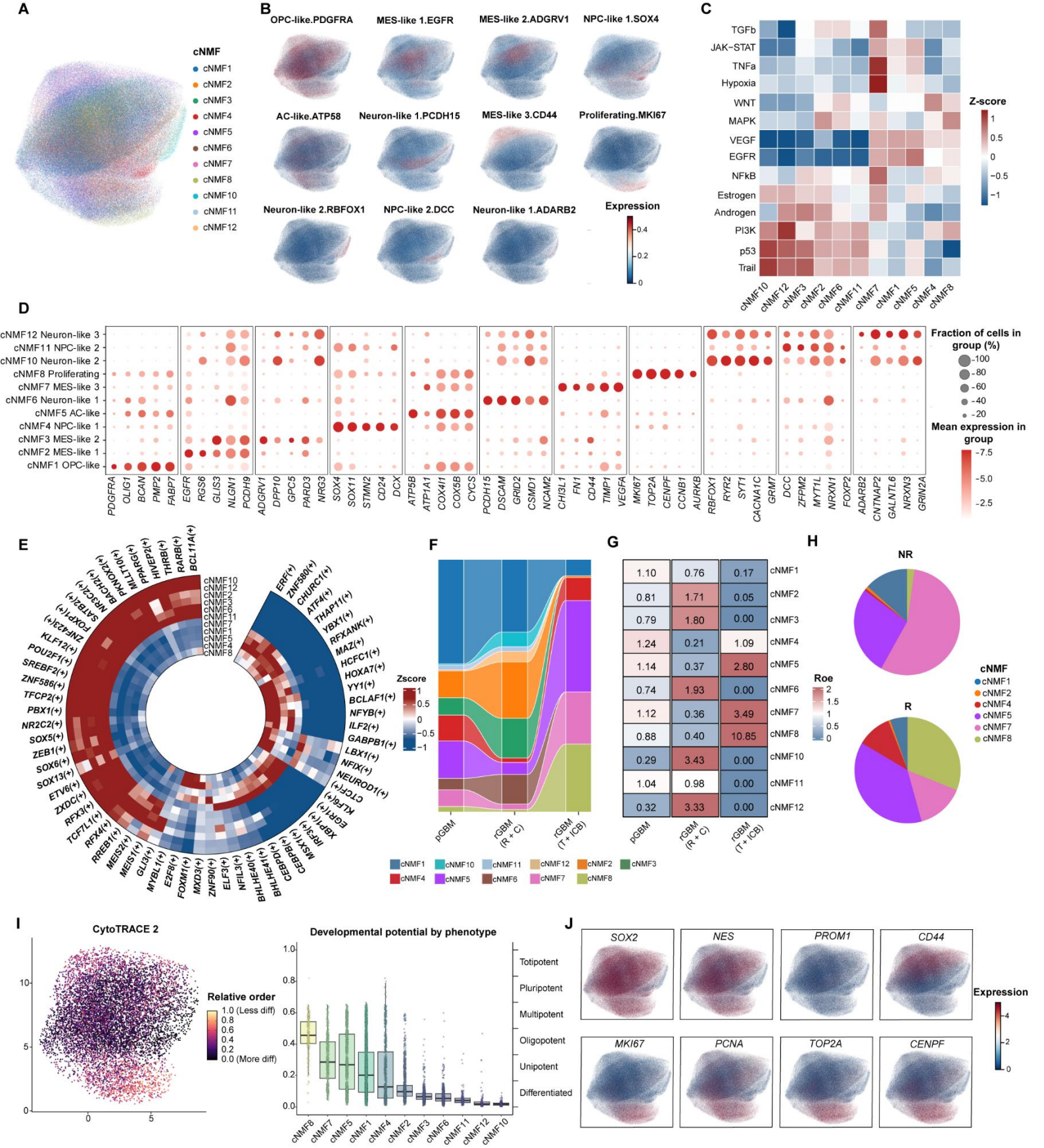

Figure 2 Identification of therapy-driven malignant states and evolutionary trajectories in GBM.

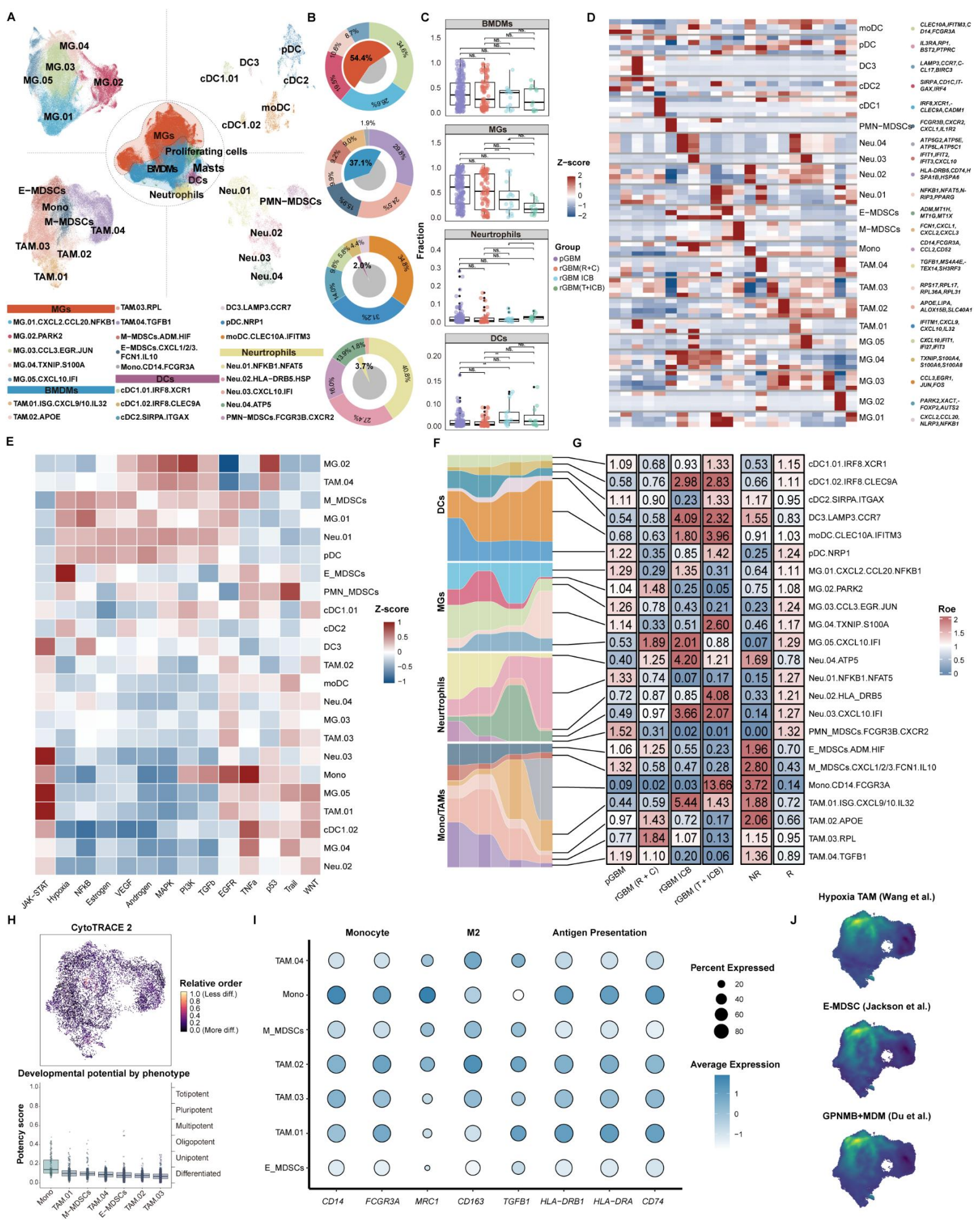

Figure 3 Hierarchy, functional heterogeneity, and therapy-induced remodeling of the myeloid compartment.

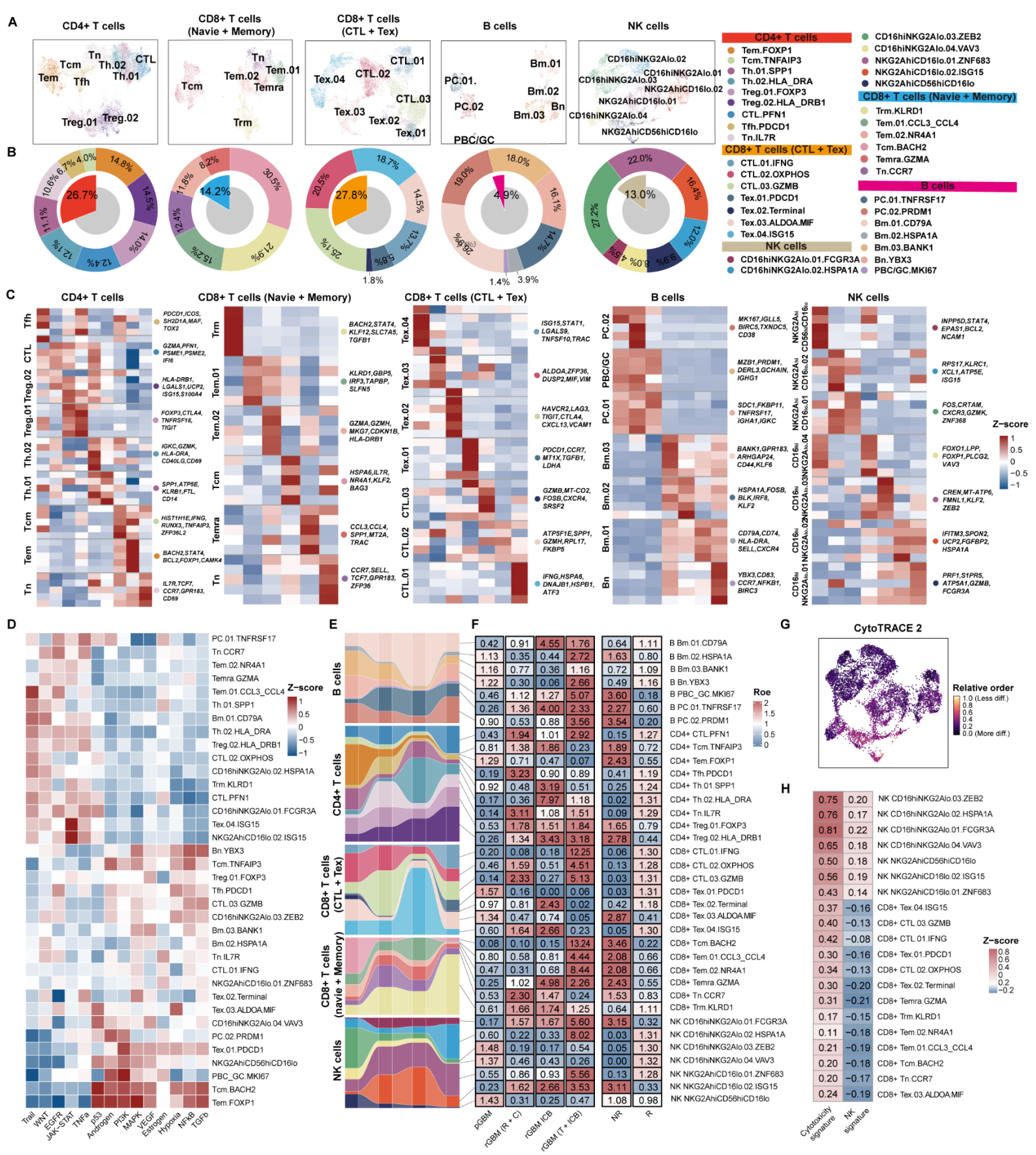

Figure 4 Divergent functional states and treatment-associated dynamics of T and NK lymphocytes.

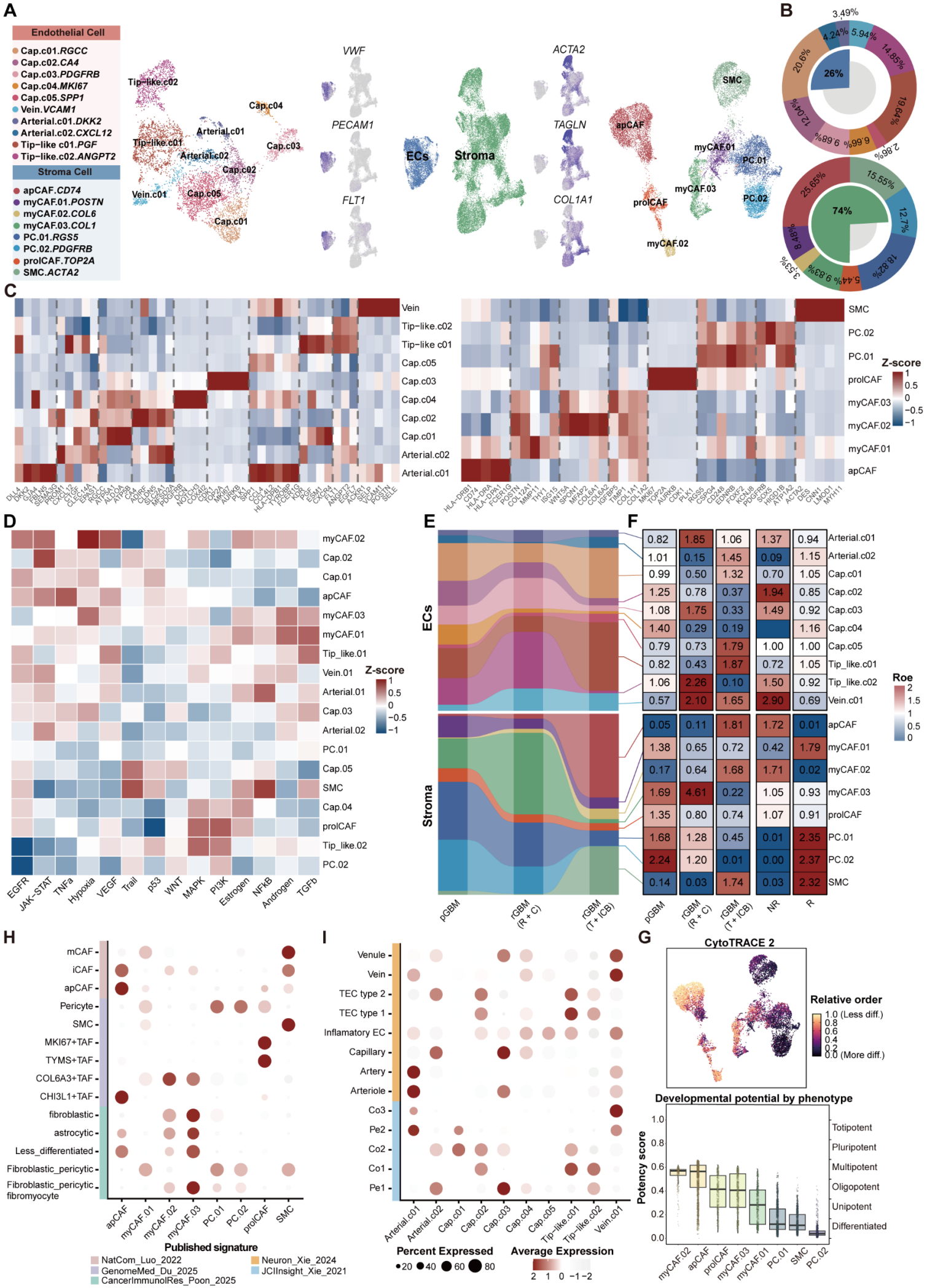

Figure 5 Remodeling of the perivascular and stromal niche under therapeutic pressure.

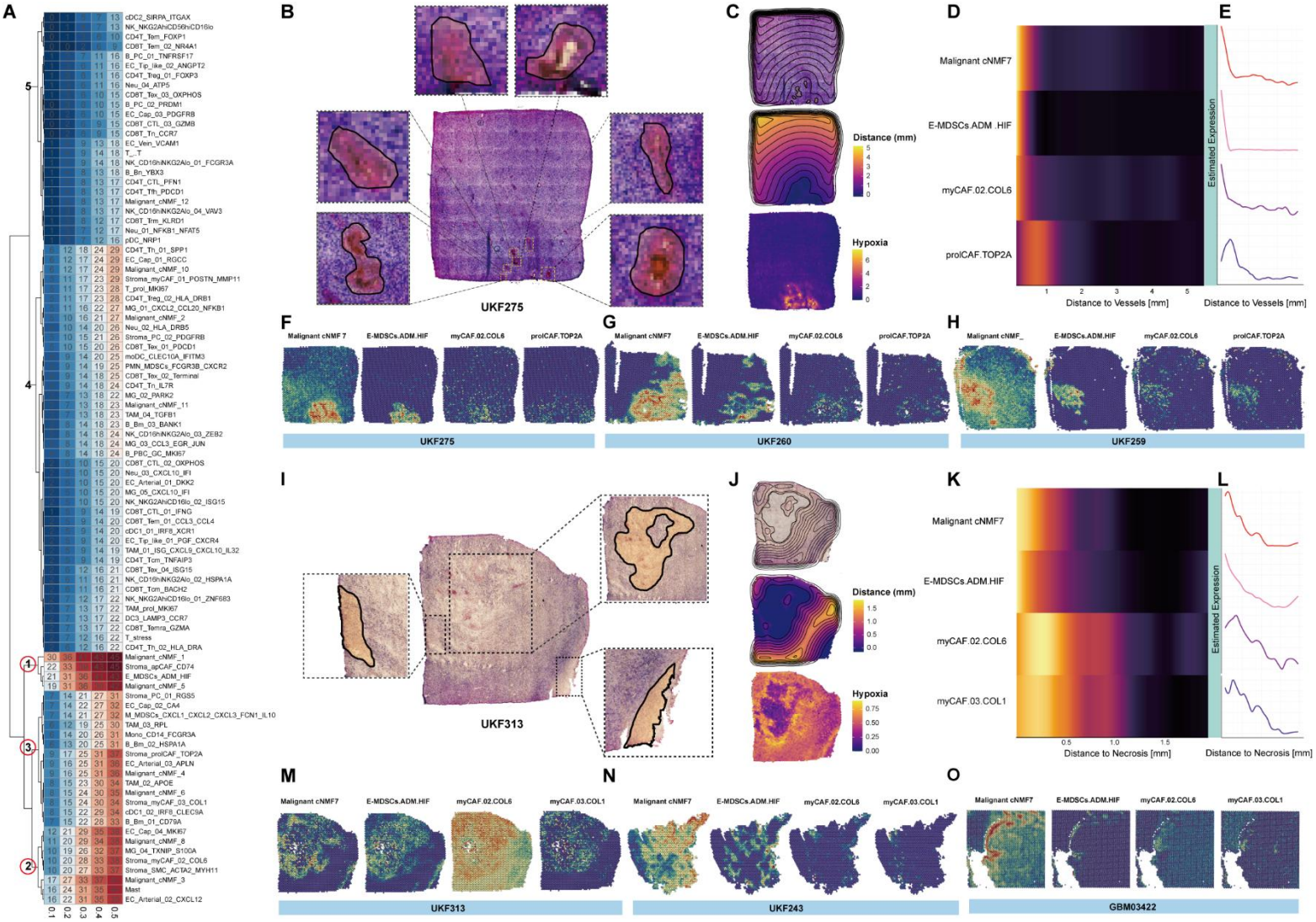

Figure 6 Spatial phylogeography defines a recurrent "Spatial Resistance Triad" within hypoxic niches.

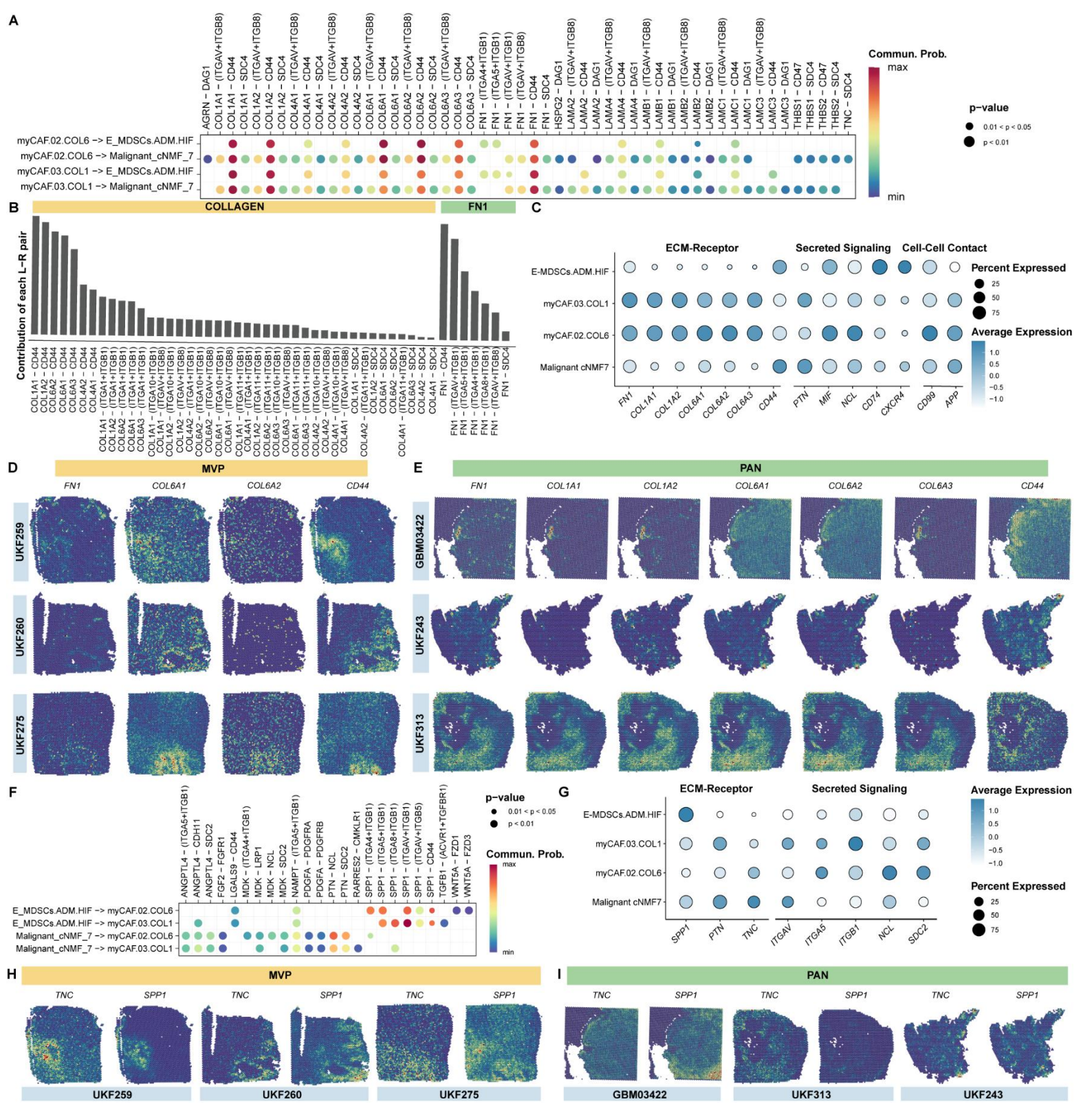

Figure 7 The ECM-CD44 axis and reciprocal paracrine signaling sustain the Spatial Resistance Triad.